



# Synergistically modulating *d*-band centers of bimetallic elements for activating cobalt atoms and promoting water dissociation toward accelerating alkaline hydrogen evolution

Shu-Ming Li<sup>b,1</sup>, Zhan Liu<sup>b,1</sup>, Xiao-Yun Li<sup>c</sup>, Cui-Fang Ye<sup>d</sup>, Yu Li<sup>b</sup>, Jin-Ping Liu<sup>a</sup>, Shen Yu<sup>b</sup>, Ming-Hui Sun<sup>b</sup>, Li-Hua Chen<sup>b,\*</sup>, Bao-Lian Su<sup>b,e,\*\*</sup>, Yi-Long Wang<sup>a,\*</sup>

<sup>a</sup> School of Chemistry, Chemical Engineering and Life Science, Wuhan University of Technology, Wuhan, Hubei 430070, China

<sup>b</sup> State Key Laboratory of Advanced Technology for Materials Synthesis and Processing, Wuhan University of Technology, Wuhan, Hubei 430070, China

<sup>c</sup> State Key Laboratory of Silicate Materials for Architectures, Wuhan University of Technology, Wuhan, Hubei 430070, China

<sup>d</sup> Department of Histology and Embryology, Tongji Medical College, Huazhong University of Science and Technology, Wuhan, Hubei 430030, China

<sup>e</sup> Laboratory of Inorganic Materials Chemistry (CMI) University of Namur, 61 rue de Bruxelles, Namur 5000, Belgium

## ARTICLE INFO

### Keywords:

Cobalt single atoms  
Ru nanoclusters  
Activating cobalt sites  
Promoting water dissociation  
Electrocatalysis

## ABSTRACT

It is of great significance to synergistically modulate *d*-band centers ( $\epsilon_d$ ) of multiple transition metals (TMs) for designing and developing highly efficient hybridized-electrocatalysts. Herein, the downshift in Co  $\epsilon_d$  is realized by synthesizing Co single atoms with low nitrogen-coordination number (CoN<sub>2</sub>) at high *T* during the pyrolysis step while upshifting Ru  $\epsilon_d$  is achieved via decreasing Ru precursor mass to anchor Ru nanoclusters instead of nanoparticles on CoN<sub>2</sub>-containing carbon substrates (CoN<sub>2</sub>/Ru-NC). In our strategy, the downshift in Co  $\epsilon_d$  leads to a favorable affinity between Co sites of CoN<sub>2</sub>/Ru-NC and H<sup>+</sup> for desorption of H<sub>2</sub>; additionally, upshifting Ru  $\epsilon_d$  helps the adsorption of OH<sup>\*</sup> intermediates on Ru nanoclusters for CoN<sub>2</sub>/Ru-NC to promote water dissociation toward accelerating alkaline producing H<sub>2</sub>. In consequence, CoN<sub>2</sub>/Ru-NC demonstrates an outstanding activity with an ultralow overpotential of ~ 9.0 mV at 10.0 mA cm<sup>-2</sup>, which suppresses activities of Pt/C (24.0 mV) and most previously-reported Ru-based electrocatalysts.

## 1. Introduction

Electrocatalytic hydrogen evolution is one of the most efficient techniques to alleviate the global energy crisis, carbon emission as well as environmental problems [1–8]. Ideal electrocatalyst not only minimizes the energy consumption but also enhances the efficiency of overall water splitting [9–24]. The rational material design is crucial to develop an efficient electrocatalyst besides the systematic experimental investigation, which is beneficial to construct a bridge between its microstructure and performance in advance [25–31]. In 1995, the *d*-band center theory proposed by Nørskov et. al. reveals the catalytic activity of the transition metals-based catalysts from the aspects of energy level change and electronic structure [32]. It can be explained as follows: the adsorption and desorption capabilities toward hydrogen-containing

intermediates depends on the position of the *d*-band center ( $\epsilon_d$ ) of the transition metals (TMs) [33–35]. Therefore, the rational regulation of  $\epsilon_d$  for designing high-performance electrocatalyst has attracted considerable interest all over the world.

Up till now, a variety of techniques have been developed to modulate  $\epsilon_d$  of TMs for the advancement of electrocatalysis, such as heteroatom doping [36], vacancy [37] and strain engineering [38], alloying [39], catalyst-substrate effect, and so on [40]. For example, phosphorus atoms have been successfully doped into atomic Pt sites with nitrogen-coordination on carbon substrates (PtNPC) for the downshift of the Pt  $\epsilon_d$  owing to the localized asymmetric structure [41]. Interestingly, this strategy weakens the binding Pt atoms to OH<sup>\*</sup> intermediates, thereby lowering the energy barrier of the rate-determining step and enhancing electrocatalytic activity of PtNPC. In addition, to quicken

\* Corresponding authors.

\*\* Corresponding author at: State Key Laboratory of Advanced Technology for Materials Synthesis and Processing, Wuhan University of Technology, Wuhan, Hubei 430070, China.

E-mail addresses: [chenlihua@whut.edu.cn](mailto:chenlihua@whut.edu.cn) (L.-H. Chen), [baoliansu@whut.edu.cn](mailto:baoliansu@whut.edu.cn) (B.-L. Su), [wangyilong@whut.edu.cn](mailto:wangyilong@whut.edu.cn) (Y.-L. Wang).

<sup>1</sup> These authors contribute equally to this paper.

electrode kinetics, abundant oxygen (O) vacancies have been dexterously introduced into the necklace-like hollow structure spinel oxides for excellent overall water splitting [42]. Introducing O vacancies results in the spin polarization of Co and its *d*-orbitals shifts to the low-energy direction, thus improving the water electrolysis [42]. In our recently-reported work, the Mo  $\epsilon_d$  of  $[\text{Mo}_3\text{S}_{13}]^{2-}$  clusters anchored on carbon cloth (CC) has been adjusted from catalyst-substrate effect toward boosting highly active defect Mo<sup>V</sup> sites [40]. Our finding clearly elucidates that electrochemically oxidizing CC at low potential can realize an upshift in the Mo  $\epsilon_d$  to increase intrinsic activity of amorphous molybdenum sulfide for hydrogen evolution reaction (HER). To the best of our knowledge, alkaline HER is the most likely for industrial hydrogen production because of the unlimited reactant availability, desired safety and adequate production [9,43]. Nevertheless, alkaline HER kinetics is 2 ~ 3 orders of magnitude lower than acidic one. It is attributed to the multi-step reaction pathways, such as the Volmer-Heyrovsky and Volmer-Tafel steps, where the sluggish Volmer stage ( $\text{H}_2\text{O} + \text{e}^- \rightarrow \text{H}_{\text{ad}} + \text{OH}^-$ ) greatly imposes restrictions on the total kinetics [44–46]. In consequence, it is quite challenging to synergistically modulate  $\epsilon_d$  of multiple TMs for simultaneously realizing desirable hydrogen atoms adsorption free energy change ( $\Delta G_{\text{H}}$ ) as well as accelerated water dissociation, even efficient charge transfer toward alkaline HER.

Herein, we have proposed a feasible strategy to synthesize Ru nanoclusters anchoring on carbon substrates which contains Co single atoms with low nitrogen-coordination number ( $\text{CoN}_2/\text{Ru-NC}$ ) to simultaneously activate Co atoms as catalytically newborn sites as well as promote water dissociation toward accelerated alkaline HER. In this strategy, the as-synthesized samples are successfully synthesized by the pyrolysis of bimetallic Co/Zn Zeolitic imidazolate frameworks (ZIFs) followed by a hydrogen/argon annealing. More importantly, the  $\epsilon_d$  of Co and Ru of the as-synthesized samples can be synergistically modulated for highly efficient alkaline HER. For example, compared to the counterpart with high nitrogen-coordination number ( $\text{CoN}_4/\text{Ru-NC}$ ), the downshift in the Co  $\epsilon_d$  of  $\text{CoN}_2/\text{Ru-NC}$  is realized by the synthesis of Co single atoms with low nitrogen-coordination number ( $\text{CoN}_2$ ) at increasing *T* during the pyrolysis step. Instead, the upshift in the Ru  $\epsilon_d$  is carried out *via* decreasing the Ru precursor mass ( $m_{\text{Ru}}$ ) to anchor Ru nanoclusters rather than nanoparticles on  $\text{CoN}_2$ -containing carbon substrates. Our data reveal that a downshift in the Co  $\epsilon_d$  leads to a favorable affinity between Co single atoms (Co-SAs) of  $\text{CoN}_2/\text{Ru-NC}$  and  $\text{H}^*$  for desorption of  $\text{H}_2$ ; on the other hand, an upshift in the Ru  $\epsilon_d$  of  $\text{CoN}_2/\text{Ru-NC}$  favors the adsorption of  $\text{OH}^*$  intermediates on Ru nanoclusters to promote water dissociation for alkaline HER. Last but not least, efficient charge transfer of the as-synthesized samples can be rationally explicated the following aspects: highly conducting carbon substrates are served as “high-way” to accelerate electron transfer for cathode kinetics; the other is that the significant electron accumulation at the interfaces between Co-SAs and Ru nanoclusters is also advantageous for further improving in charge transfer during HER. With these benefits,  $\text{CoN}_2/\text{Ru-NC}$  demonstrates an outstanding HER activity with an ultralow overpotential of ~ 9.0 mV at the current density of 10.0 mA cm<sup>-2</sup> and Tafel plot of 45 mV dec<sup>-1</sup> in alkaline environments, which is superior to activities of Pt/C and most previously-reported Ru-based electrocatalysts. Our results promise potential applications in electrocatalysis or energy conversion.

## 2. Experimental section

### 2.1. Synthesis of bimetallic Co/Zn ZIFs

5.580 g of Zn ( $\text{NO}_3$ )<sub>2</sub>·6 H<sub>2</sub>O and 2.730 g of Co( $\text{NO}_3$ )<sub>2</sub>·6 H<sub>2</sub>O are dissolved into 150.0 mL methanol, and then, this solution is added into 150.0 mL of methanol solution containing 6.160 g of 2-methylimidazole at magnetic stirring. The above mixture is stirred at 25 °C for 8.0 h. After that, this precipitate is centrifuged and rinsed with methanol five times.

Subsequently, it is dried in the vacuum at 80 °C for 12.0 h.

### 2.2. Synthesis of Co-SAs

The as-obtained Zn/Co-ZIFs is pyrolyzed under an argon atmosphere in a tube oven, kept at 800 °C for 1.0 h, 900 °C for 1.0 h and 1000 °C for 1.0 h with the heat rate of 5 °C min<sup>-1</sup>, respectively. Then, it is cooled to about 25 °C. The as-pyrolyzed sample is directly used without any post-treatment and denoted as  $\text{CoN}_2$ . In addition, Co-SAs with high nitrogen-coordination number (to be denoted as  $\text{CoN}_4$ ) are pyrolyzed at 800 °C for 3.0 h under otherwise the same conditions.

### 2.3. Synthesis of Ru nanoclusters anchoring on carbon substrates which contains $\text{CoN}_2$ ( $\text{CoN}_2/\text{Ru-NC}$ )

30 mg of  $\text{RuCl}_3 \cdot x\text{H}_2\text{O}$  is dissolved into 10.0 mL of deionized water. Subsequently, 120 mg of the as-obtained  $\text{CoN}_2$  is well dispersed into this Ru precursor solution under the sonication for 0.5 h to gain the as-synthesized suspensions. The related precipitate is obtained by centrifuging, washing with deionized water for 3 times and drying at 60 °C for 24.0 h, respectively. To obtain the as-synthesized sample, the precipitate is calcinated at 300 °C for 2.0 h with the heat rate of 5 °C min<sup>-1</sup> in 10%  $\text{H}_2/\text{Ar}$  mixed gas. And it is denoted as  $\text{CoN}_2/\text{Ru-NC}$  and directly used without any post-treatment.

### 2.4. Synthesis of Ru nanoparticles anchoring on carbon substrates which contains $\text{CoN}_2$ ( $\text{CoN}_2/\text{Ru-NP}$ )

The synthesis of  $\text{CoN}_2/\text{Ru-NP}$  is the same as that of  $\text{CoN}_2/\text{Ru-NC}$  except for 90 mg of  $\text{RuCl}_3 \cdot x\text{H}_2\text{O}$  rather than 30 mg.

### 2.5. Synthesis of Ru nanoclusters anchoring on carbon substrates which contains $\text{CoN}_4$ ( $\text{CoN}_4/\text{Ru-NC}$ )

The synthesis of  $\text{CoN}_4/\text{Ru-NC}$  is the same as that of  $\text{CoN}_2/\text{Ru-NC}$  except for the presence of  $\text{CoN}_4$  rather than  $\text{CoN}_2$ .

### 2.6. Pretreatment of Ni foam (NF)

The pretreatment of NF is conducted according to our previously-reported work [9].

### 2.7. Characterization

The microstructures and morphology of all samples are detected by a field emission scanning electron microscopy (FESEM, Hitachi S-4800, 5 kV) and a high-resolution transmission electron microscope (HRTEM, JEOL JEM-2100 F, 200 kV). Inductively coupled plasma atomic emission spectroscopy (ICP-AES, Optima 7300 DV) is utilized to determine the concentration of Co and Ru species. The crystal phases and chemical compositions of the as-synthesized samples are recognized by a powder X-ray diffraction (XRD, Bruker AXS D8-Advance) patterns, a diffractometer with Cu K $\alpha$  radiation ( $\lambda = 0.15418$  nm) in the 2 $\theta$  range from 5 ° to 60 ° at a scanning step of 0.05 °. The high-angle annular dark-field scanning transmission electron microscopy (HAADF-STEM) images are identified by a high-resolution transmission electron microscopy (Titan Cubed Themis G2 300 working at 300 kV), equipped with a probe spherical aberration corrector. Elemental mapping results of all samples are obtained by the HAADF-STEM mode combination with energy-dispersive X-ray spectroscopy (EDX) analysis. The elemental composition of bimetallic Co/Zn ZIFs is characterized by an EDX associated with FESEM. X-ray photoelectron spectroscopy (XPS) measurements are performed on a VG Multilab 2000 X with an Al K $\alpha$  radiation as the excitation source. Zeta potential measurements are carried out using Zetasizer Nano ZS90 device by Malvern Instruments [9]. Co and Ru K-edge X-ray absorption near-edge structure (XANES) measurements are

provided in [Supplementary Material](#).

## 2.8. Electrochemical measurements

Each sample is performed as the corresponding electrocatalyst pasted on the glassy carbon electrode (GCE, 3 mm in diameter) as the working electrode. To prepare the related working electrodes, 10 mg of the as-synthesized sample is mixed in a solution consisting of 880  $\mu\text{L}$  isopropanol, 100  $\mu\text{L}$  deionized water and 20  $\mu\text{L}$  5.0 wt% nafion solution to prepare the corresponding inks. After the ultrasonic treatment for 30 min, 5  $\mu\text{L}$  of the resulting ink is pasted on GCE and dried for a while.

Electrochemical measurements are conducted in a typical three-electrode systems on a CHI 660E electrochemical workstation (Shanghai Chenhua Instruments, China) at the room temperature. Meanwhile, a graphite rod and an Hg/HgO electrode (saturated KOH solution) are employed as the counter electrode and as the reference electrode, respectively. In this work, the potentials *versus* the reversible hydrogen electrode (RHE) have been utilized in all electrochemical measurements by the following equation:

$$E(\text{RHE}) = E(\text{Hg/HgO}) + 0.0591 \times \text{pH} + 0.098$$

Polarization curves are measured at a scan rate of 5  $\text{mV s}^{-1}$  with 90 % iR compensations, which is recorded from 0 to  $-0.4 \text{ V}$ . The Tafel slopes are obtained according to the Tafel equation ( $\eta = a + b \log(j)$ ). The Nyquist plots are deceted with frequency between 100 kHz and 0.01 Hz at a potential of  $-0.02 \text{ V}$ . The impedance results are fitted into the simplified Randles circuit to excerpt the series and charge transfer resistance ( $R_{\text{CT}}$ ). The electrochemical active surface area is characterized by measuring double layer capacitance ( $C_{\text{dl}}$ ) of the as-synthesized samples in the non-Faraday potential range originated from the cyclic voltammetry (CV) curves. The CV curves are detected at the scan rates of 10.0, 20.0, 30.0, 40.0, 50.0, 60.0, 70.0, 80.0, 90.0 and 100.0  $\text{mV s}^{-1}$  in varying from  $-0.024$  to  $0.424 \text{ V}$ , respectively. As for the stability tests

and the cycling performance, 100  $\mu\text{L}$  ink is dispersed onto the pre-treated NF ( $1.0 \times 1.0 \text{ cm}^2$ ). The stability tests are measured by current *versus* time (i-t) chronoamperometric signal at a current density of  $10 \text{ mA cm}^{-2}$  for 24 h. Additionally, the cycling performance of the working electrode is evaluated by repeating linear sweep voltammetry for 4000 cycles. All electrochemical measurements are conducted in the electrolyte of 1.0 M KOH bubbled with  $\text{N}_2$  without an activation process.

## 2.9. Theoretical calculations

First-principle calculations are conducted by the density functional theory (DFT) to assess HER activity of the as-synthesized samples [11]. On the other hand, the adsorption energies of the water ( $\Delta E_{\text{ads}}$ ) as well as the dissociation energy barriers of the water molecule on the surfaces of  $\text{CoN}_2/\text{Ru-NC}$ ,  $\text{CoN}_2/\text{Ru-NP}$  and  $\text{CoN}_4/\text{Ru-NC}$  are calculated in terms of our previously-reported work [9].

## 3. Results and discussion

In modelling, the nitrogen-doped (N-doped)  $\text{sp}^2$  carbon layers are taken as substrates [25,47,48]. According to the following Co K-edge X-ray absorption near-edge structure (XANES) spectra and the corresponding fittings in this work, the number of low and high nitrogen-coordination for Co-SAs are set as 2 and 4 for constructing the related models, respectively. The atom number of Ru nanoclusters (Ru-NC) in the models of  $\text{CoN}_2/\text{Ru-NC}$  or  $\text{CoN}_4/\text{Ru-NC}$  is fixed to 22 while that of Ru nanoparticles (Ru-NP) is set as 42 in  $\text{CoN}_2/\text{Ru-NP}$  model. In the latter model, we select three layers of Ru atoms on the (002) plane for modeling Ru-NP of  $\text{CoN}_2/\text{Ru-NP}$  based on its XRD pattern in this work. Subsequently, the schematic illustration of  $\text{CoN}_2/\text{Ru-NC}$ ,  $\text{CoN}_2/\text{Ru-NP}$  and  $\text{CoN}_4/\text{Ru-NC}$  models is presented in Fig. 1a–c for the calculations of  $\Delta G_{\text{H}}$ . Site 1 in all models represents Co-SAs adjacent to Ru nanoclusters (Ru-NC) or Ru nanoparticles (Ru-NP). Site 2 represents Ru atom of Ru-NC or Ru-NP away from

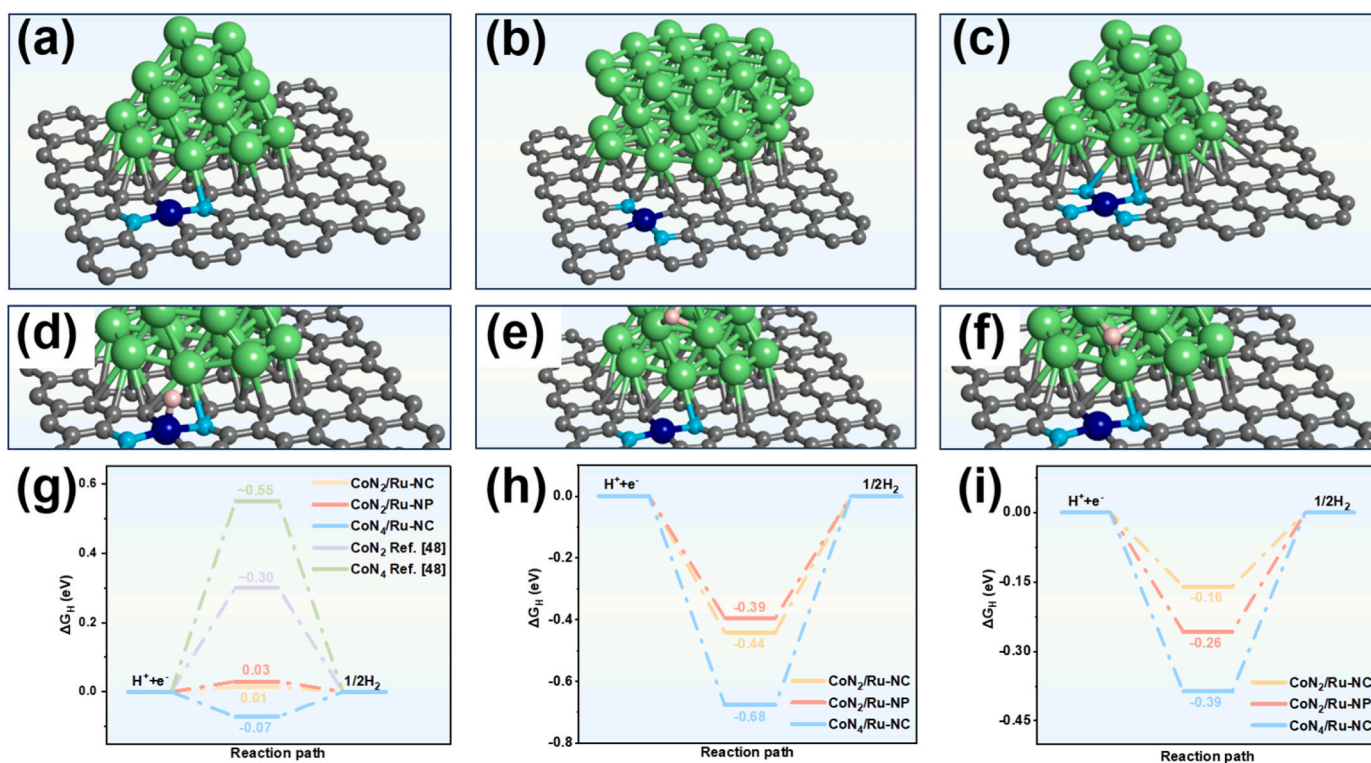


**Fig. 1.** Schematic illustration of (a)  $\text{CoN}_2/\text{Ru-NC}$ , (b)  $\text{CoN}_2/\text{Ru-NP}$  and (c)  $\text{CoN}_4/\text{Ru-NC}$  models for the calculations of  $\Delta G_{\text{H}}$ ; Schematic illustration of (d) sites 1, (e) 2 and (f) 3 for the absorption of H atom on  $\text{CoN}_2/\text{Ru-NC}$ ;  $\Delta G_{\text{H}}$  at (g) sites 1, (h) 2 and (i) 3 of all models. In (a-c), the blue balls are Co atoms while green balls are Ru atoms, gray balls for C atoms and cyan balls for N atoms. In (d), (e) and (f), light pink balls are H atoms.



Co-SAs while site 3 does Ru atom at located between Co-SAs and Ru-NC or Ru-NP (or to be called as interfaces). Fig. 1d–f, and Fig. S1, 2 display sites 1, 2 and 3 of CoN<sub>2</sub>/Ru-NC, CoN<sub>2</sub>/Ru-NP and CoN<sub>4</sub>/Ru-NC models. Following the above models, Fig. 1g–i present the theoretical  $\Delta G_H$  at these sites for the prediction of HER activity. The detailed results are listed in Table S1, yielding the data ranging from  $-0.68$  to  $0.01$  eV. According to the previously-reported literature,  $\Delta G_H$  at Co atoms of CoN<sub>2</sub> and CoN<sub>4</sub> reaches up to  $\sim 0.30$  and  $\sim 0.50$  [48], respectively, implying the unsatisfactory HER nature at the absence of Ru species. In comparison, while by anchoring Ru-NC or Ru-NP on Co-SAs-containing carbon substrates,  $\Delta G_H$  at site 1 of CoN<sub>2</sub>/Ru-NC, CoN<sub>2</sub>/Ru-NP and CoN<sub>4</sub>/Ru-NC greatly decrease to  $0.01$ ,  $0.03$  and  $-0.07$  eV, respectively (Fig. 1g). As is shown in Fig. 1h,  $\Delta G_H$  at sites 2 of all models range from  $-0.68$  to  $-0.39$ . Additionally,  $\Delta G_H$  at interfaces between Co-SAs and Ru-NC or Ru-NP (site 3) reach to  $-0.16$  eV for CoN<sub>2</sub>/Ru-NC,  $-0.26$  eV for CoN<sub>2</sub>/Ru-NP and  $-0.39$  eV for CoN<sub>4</sub>/Ru-NC (Fig. 1i). These results straightforwardly disclose that neither site 2 (Ru atom) nor site 3 (interfaces) is catalytically active for HER. Instead, site 1 might be real catalytic center. Even more importantly is,  $\Delta G_H$  at site 1 of CoN<sub>2</sub>/Ru-NC is closer to zero (about  $0.01$ ) than that of

CoN<sub>2</sub>/Ru-NP or CoN<sub>4</sub>/Ru-NC. As a result, we can reasonably deduce that CoN<sub>2</sub>/Ru-NC could exhibit the highest HER activity among all samples.

Guided by the above DFT calculations, we have developed a feasible strategy for a pyrolysis of bimetallic Co/Zn ZIFs followed by the hydrogen/argon annealing to synthesize CoN<sub>2</sub>/Ru-NC and CoN<sub>4</sub>/Ru-NC (Fig. S3). In this strategy, changing  $T$  at the pyrolysis step can regulate the nitrogen-coordination number of Co-SAs [48,49], that is, high  $T$  pyrolysis for the synthesis of CoN<sub>2</sub>, and low  $T$  pyrolysis for that of CoN<sub>4</sub> (Fig. S3). On the other hand, low  $m_{Ru}$  (about 30 mg) tends to anchor Ru-NC on CoN<sub>2</sub>-containing carbon substrates to synthesize CoN<sub>2</sub>/Ru-NC while increasing  $m_{Ru}$  to ca. 90 mg can anchor Ru-NP instead of Ru-NC on such substrates to obtain CoN<sub>2</sub>/Ru-NP. Expectedly, after low  $T$  pyrolysis of Co/Zn ZIFs, we can synthesize CoN<sub>4</sub>/Ru-NC at low  $m_{Ru}$  (Fig. S3).

As is shown in SEM (Fig. 2a) and TEM (Fig. 2b) images, CoN<sub>2</sub>/Ru-NC inherits the morphology of ZIFs (Figs. S4, 5) [48], each dodecahedron with a diameter of approximately 500 nm. No nanoparticle aggregation can be observed on the surface of CoN<sub>2</sub>/Ru-NC. From Fig. S6a, CoN<sub>2</sub>/Ru-NP almost exhibits the same morphology as

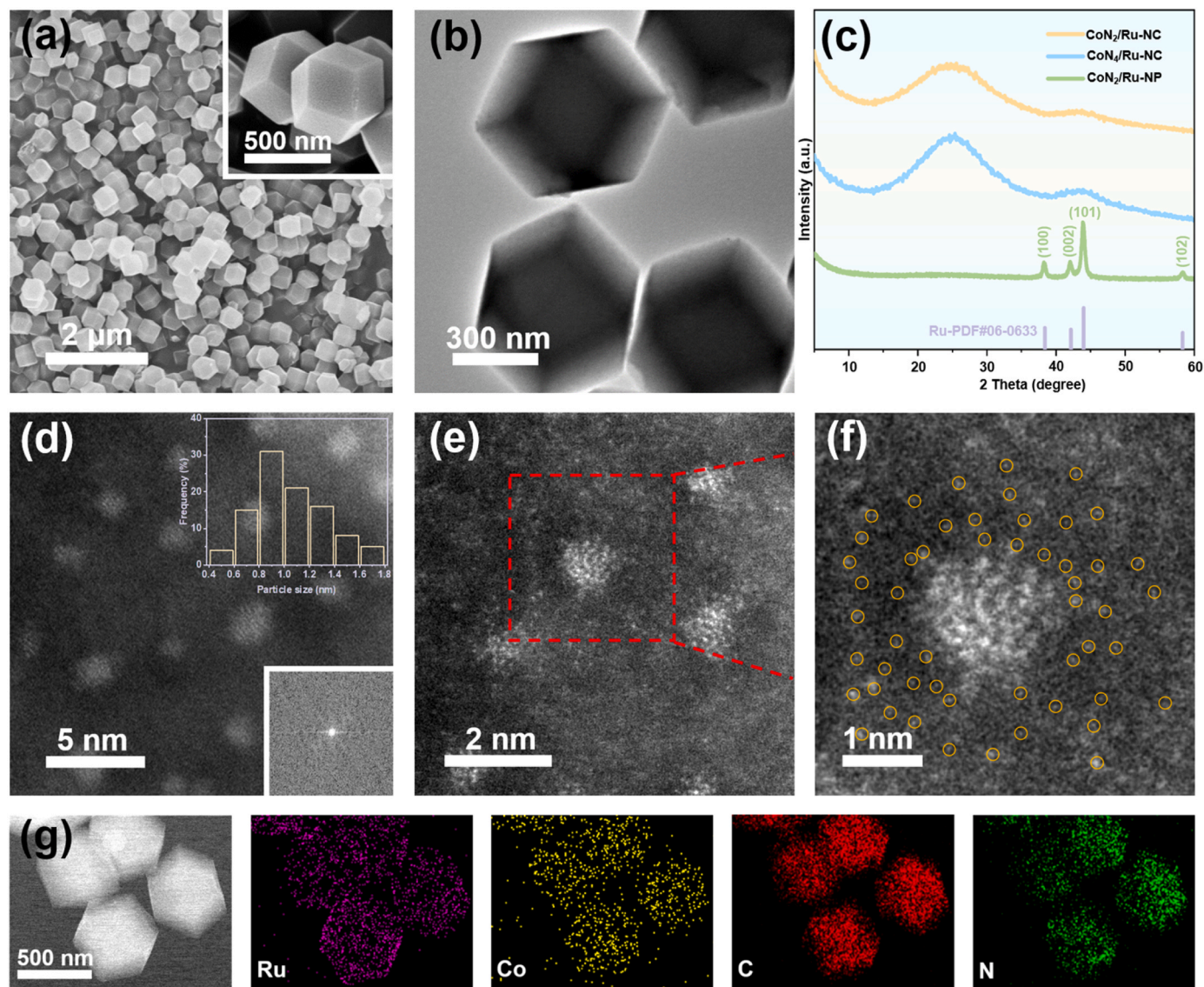


**Fig. 2.** (a) SEM, (b) TEM and (d–f) HAADF-STEM images of CoN<sub>2</sub>/Ru-NC; (c) XRD patterns of CoN<sub>2</sub>/Ru-NC, CoN<sub>4</sub>/Ru-NC and CoN<sub>2</sub>/Ru-NP; (g) HAADF-STEM-EDX mappings of Ru, Co, C and N over CoN<sub>2</sub>/Ru-NC. (f) is the magnified image of the red dotted frame indicated in (e). Inset of (a) is the magnified SEM image of CoN<sub>2</sub>/Ru-NC. The upper and lower insets of (d) are diameter distribution histogram of Ru-NC in CoN<sub>2</sub>/Ru-NC and FFT pattern of (d), respectively.



CoN<sub>2</sub>/Ru-NC. Differently, some nanoparticles exist on the surface of CoN<sub>2</sub>/Ru-NP from the magnified SEM image (inset of Fig. S6a) and TEM images (Fig. S6b, c). It is observed that nanoparticles with an average diameter of about 5.2 nm are distributed on the carbon substrates (inset of Fig. S6c). Additionally, the concentrations (C) of Co and Ru species of CoN<sub>2</sub>/Ru-NC are 0.9 and 1.5 wt%, respectively, which is characterized by ICP-AES. There is no significant diffraction peak about metallic Co or Ru except broad peaks of the graphitized carbon (PDF#26-1076) from the XRD patterns of CoN<sub>2</sub>/Ru-NC and CoN<sub>4</sub>/Ru-NC (Fig. 2c), indicating that both Co and Ru species of these samples are amorphous. Instead, the diffraction peaks of CoN<sub>2</sub>/Ru-NP (Fig. 2c) located at  $2\theta$  of 38.5, 42.2, 44.0 and 58.4 ° match exactly the (100), (002), (101) and (102) planes of Ru (PDF#06-0663), respectively. Subsequently, HAADF-STEM images directly demonstrate the atomic dispersion of Co and Ru species in CoN<sub>2</sub>/Ru-NC because of high Z-contrasts of Co and Ru in comparison with those of C and N in Fig. 2d–f. For example, Fig. 2d show atomic-scaled nanoclusters whose average size is  $\sim 1.0$  nm through statistical measurement (upper inset of Fig. 2d). Associated with the characterizations of CoN<sub>2</sub> (Fig. S7, 8), we could hypothesize that the bright speckles indicated by yellow circles in Fig. 2f might be Co-SAs. At the same time, a lot of single atoms are adjacent to nanoclusters (Fig. 2f). From Fig. 2d–f, CoN<sub>2</sub>/Ru-NC does

not yet present any characteristic lattice spacings of metallic Co and Ru; and Fast Fourier transform (FFT) pattern (lower inset of Fig. 2d) further reveals the poor crystallinity of such Co or Ru species of CoN<sub>2</sub>/Ru-NC, being in good agreement with the XRD results (Fig. 2c). As is shown in Fig. 2g, HAADF-STEM-EDX mappings of CoN<sub>2</sub>/Ru-NC demonstrates the uniform distribution of Co, Ru, N and C elements. Based on the above analysis, CoN<sub>4</sub>/Ru-NC almost exhibits the same micro-structures as CoN<sub>2</sub>/Ru-NC (Fig. S9).

To confirm the existence of Co-SAs as well as investigate the electronic structure and coordination environment of CoN<sub>2</sub>/Ru-NC and CoN<sub>4</sub>/Ru-NC, we further characterize their high-resolution XPS and X-ray absorption fine structure (XAFS) spectra (Fig. 3). First, the C1s XPS spectra of both CoN<sub>2</sub>/Ru-NC and CoN<sub>4</sub>/Ru-NC (Fig. 3a) are deconvoluted into four characteristic peaks, being attributed to C–C, C–N, C–O and C=C [50,51]. Among them, the presence of C–N peak directly verifies N atoms successfully doping into carbon substrates [48]. Furthermore, CoN<sub>2</sub>/Ru-NC exhibits a lower C of nitrogen (7.46 at%) than CoN<sub>4</sub>/Ru-NC (19.44 at%), as listed in Table S2. Second, the N1s XPS spectrum of CoN<sub>2</sub>/Ru-NC (Fig. 3b) is divided into the pyridinic-N, Co–N and graphitic-N. For example, the characteristic peak located at the binding energy of 399.0 eV comes from the Co–N coordination between Co-SAs and N atoms [52]. CoN<sub>4</sub>/Ru-NC almost exhibits the

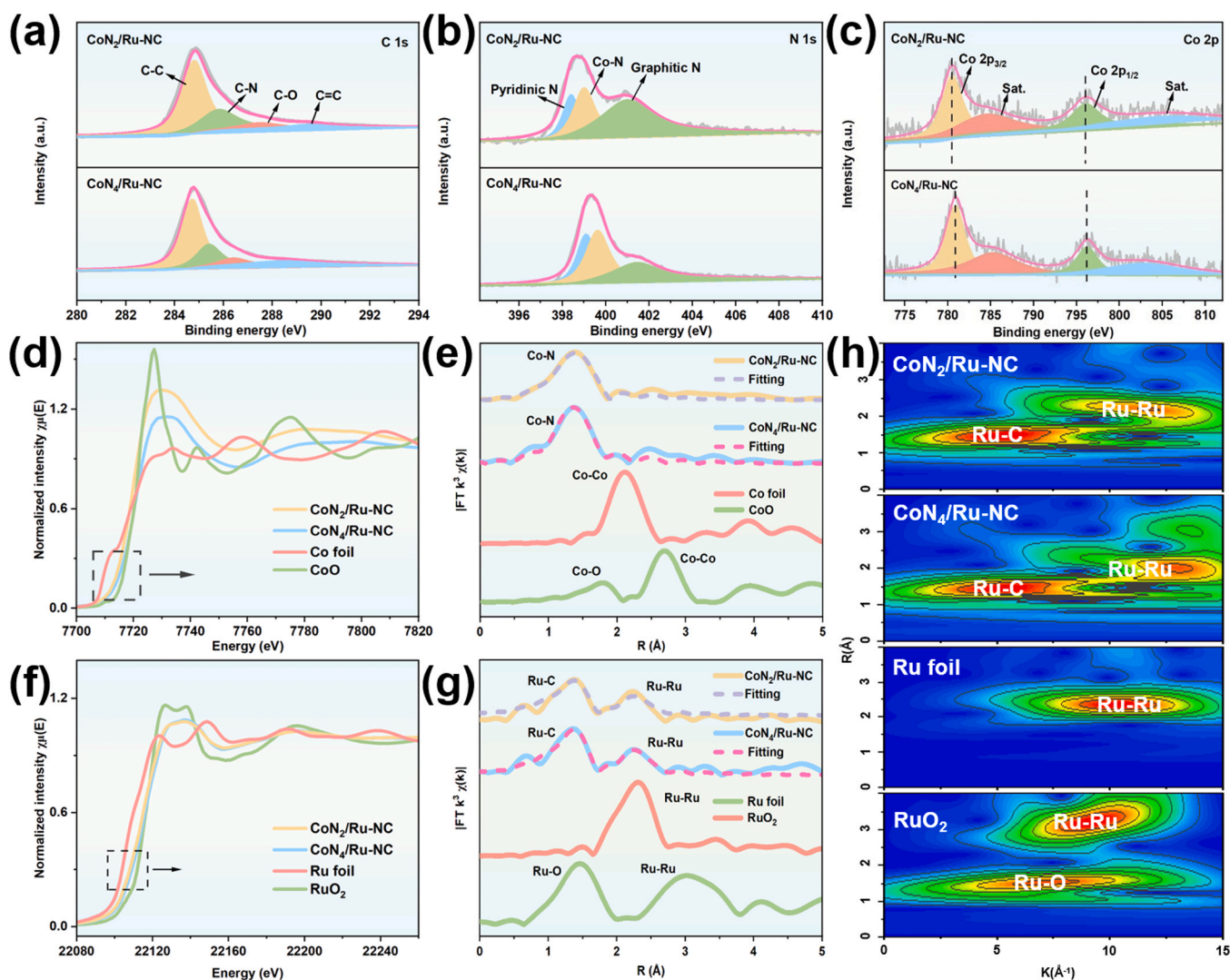


**Fig. 3.** (a) C1s, (b) N1s and (c) Co2p XPS spectra of CoN<sub>2</sub>/Ru-NC and CoN<sub>4</sub>/Ru-NC; (d) Normalized Co K-edge XANES spectra and (e) Fourier transforms  $k^3$ -weighted Co K-edge EXAFS spectra of CoN<sub>2</sub>/Ru-NC, CoN<sub>4</sub>/Ru-NC, Co foil and CoO as well as the related fitting curves; (f) Normalized Ru K-edge XANES spectra and (g) Fourier transforms  $k^3$ -weighted Ru K-edge EXAFS spectra of CoN<sub>2</sub>/Ru-NC, CoN<sub>4</sub>/Ru-NC, Ru foil and RuO<sub>2</sub> as well as the related fitting curves; (h) WT  $k^3$ -weighted Ru K-edge EXAFS signals of CoN<sub>2</sub>/Ru-NC, CoN<sub>4</sub>/Ru-NC, Ru foil and RuO<sub>2</sub>.

same N1s XPS spectrum as CoN<sub>2</sub>/Ru-NC (Fig. 3b). Third, the doublet peaks at 780.5 and 796.0 eV match well the characteristic ones of Co<sup>2+</sup> 2p<sub>3/2</sub> and 2p<sub>1/2</sub>, respectively, while the other two peaks are ascribed to the satellite peaks of Co<sup>2+</sup> 2p (Fig. 3c) [52,53]. The signal about metallic cobalt is not found yet, coinciding well with the results of the XRD

pattern (Fig. 2c). Particularly, the indispensable peaks about Co species of CoN<sub>2</sub>/Ru-NC (Fig. 3c) downshift to the low binding energies of 780.5 and 796.0 eV in comparison with those of CoN<sub>4</sub>/Ru-NC (780.8 and 796.2 eV), which manifests that CoN<sub>2</sub>/Ru-NC presents a lower valence of Co element than CoN<sub>4</sub>/Ru-NC. As is shown in Fig. S10, 11, both CoN<sub>2</sub>

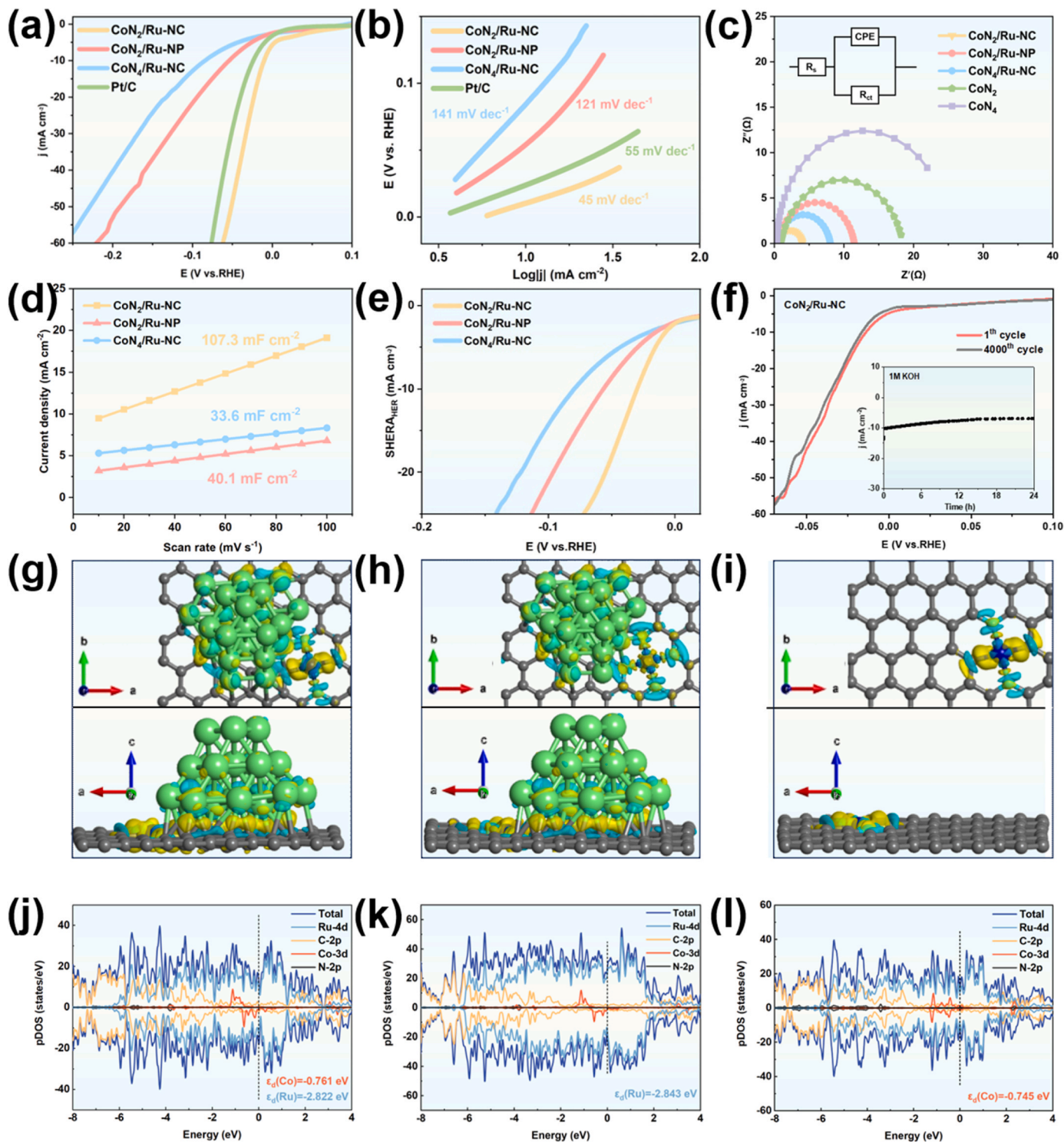


**Fig. 4.** (a) Polarization curves and (b) Tafel plots of CoN<sub>2</sub>/Ru-NC, CoN<sub>2</sub>/Ru-NP, CoN<sub>4</sub>/Ru-NC and Pt/C; (c) Nyquist plots of CoN<sub>2</sub>/Ru-NC, CoN<sub>2</sub>/Ru-NP, CoN<sub>4</sub>/Ru-NC, CoN<sub>2</sub> and CoN<sub>4</sub>; (d) C<sub>dl</sub> and (e) SHERA of CoN<sub>2</sub>/Ru-NC, CoN<sub>2</sub>/Ru-NP and CoN<sub>4</sub>/Ru-NC; (f) Polarization curves of CoN<sub>2</sub>/Ru-NC before and after 4000 cycles for a durability test; Charge density difference of top-view (upper figure) and side-view (lower figure) of (g) CoN<sub>2</sub>/Ru-NC, (h) CoN<sub>4</sub>/Ru-NC and (i) CoN<sub>2</sub> calculated at isovalue = 0.005 by the equation of  $\Delta\rho = \rho(\text{total}) - \rho(\text{Ru}) - \rho(\text{CN}) - \rho(\text{Co})$ ; DOS of (j) CoN<sub>2</sub>/Ru-NC, (k) CoN<sub>2</sub>/Ru-NP and (l) CoN<sub>4</sub>/Ru-NC. The yellow region represents the electron accumulation while the blue region represents the electrons depletion in (g–i). Inset of (f) is time-dependent current density curve of CoN<sub>2</sub>/Ru-NC for 24.0 h. All electrochemical experiments are done in a N<sub>2</sub>-saturated 1.0 mol L<sup>-1</sup> KOH solution.

and CoN<sub>4</sub> display the similar Cls, N1s and Co2p XPS spectra, further implying that Co species of CoN<sub>2</sub>/Ru–NC or CoN<sub>4</sub>/Ru–NC possess the separation property as Co–SAs.

From Co K-edge XANES spectra (Fig. 3d), the absorption edges of CoN<sub>2</sub>/Ru–NC and CoN<sub>4</sub>/Ru–NC are located between Co foil and CoO, which indicates that the average valence of these Co species locates between 0 and +2. Their Co K-edge EXAFS (Fig. S12 and Fig. 3e) spectra reveal the coordination environment of Co atoms. A prominent peak at 1.4 Å (Fig. 3e) belongs to the distance of the first Co–N shell in R space [54]. Significantly, there is no any signals at 2.1 and 1.8 Å attributed to the Co–Co bond of Co foil and Co–O bond of CoO, respectively, which evidently proves that Co species exists as Co–SAs [55]. As is listed in Table S3, the Co–N coordination number in CoN<sub>2</sub>/Ru–NC and CoN<sub>4</sub>/Ru–NC are 2.2 and 4.1, respectively. These data clearly indicate that our models about Co–SAs (Fig. 1a–c) are basically consistent with the experimental results. And it also ensures the rationality of our DFT calculations. Here, we further investigate wavelet transforms (WT) of CoN<sub>2</sub>/Ru–NC and CoN<sub>4</sub>/Ru–NC (Fig. S13). WT of CoN<sub>2</sub>/Ru–NC is almost the same as that of CoN<sub>4</sub>/Ru–NC but distinct from that of Co foil or CoO, only one intensity maximum about at 4.6 Å<sup>−1</sup> being ascribed to the Co–N bond [53]. Therefore, it can be understood that Co–SAs have successfully introduced into CoN<sub>2</sub>/Ru–NC or CoN<sub>4</sub>/Ru–NC by the pyrolysis of bimetallic Co/Zn ZIFs. That is to say, changing *T* at the pyrolysis step does regulate the coordination environment of Co–SAs of the as-synthesized samples.

There are two pairs of characteristic peaks about metallic Ru and Ru<sup>x+</sup> species [56,57] from the Ru3p XPS spectra of CoN<sub>2</sub>/Ru–NC and CoN<sub>4</sub>/Ru–NC in Fig. S14, 15. A pair of peaks about metallic Ru should be reasonably explicated as the presence of Ru atoms. Another pair of peaks attribute to Ru<sup>x+</sup>, which should originate from Ru nanoclusters anchoring on carbon substrates through the Ru–C bond [56], as described in our modelling. To verify this opinion, we further measure the Ru K-edge XANES spectra of CoN<sub>2</sub>/Ru–NC and CoN<sub>4</sub>/Ru–NC, as shown in Fig. 3f. Remarkably, their absorption edges are situated between Ru foil and RuO<sub>2</sub>. Also, their Ru K-edge EXAFS spectra (Fig. S16 and Fig. 3g) demonstrate the following two coordination types: one is that the Ru–Ru bond of Ru–NC with a peak of 2.2 Å matches the distance of the first Ru–Ru shell in the corresponding R space; the other is that the Ru–C bond with a peak of 1.4 Å is attributed to Ru atoms coordinated with substrates [58]. Considering the difficulty of EXAFS in identifying the difference between the Ru–C coordination from our samples and the Ru–O coordination from RuO<sub>2</sub> (Fig. 3g), we further employ WT analysis to distinguish this problem. Next, the contour plots of CoN<sub>2</sub>/Ru–NC and CoN<sub>4</sub>/Ru–NC, Ru foil and RuO<sub>2</sub> are shown in Fig. 3h. One intensity maximum at 12.0 Å<sup>−1</sup> in contour plot of CoN<sub>2</sub>/Ru–NC or CoN<sub>4</sub>/Ru–NC originates from the Ru–Ru bond of Ru–NC in comparison with that of RuO<sub>2</sub>, whereas the other maximum at 5.0 Å<sup>−1</sup> corresponds to the Ru–C bond instead of Ru–O one [59]. Consequently, these results clearly reveal that Ru–NC anchor on CoN<sub>2</sub>– or CoN<sub>4</sub>–containing substrates through the Ru–C bond.

A series of electrochemical properties are evaluated to HER activity of the as-synthesized samples by a typical three-electrode system (Fig. 4a–f). From Fig. 4a, CoN<sub>2</sub>/Ru–NC exhibits the optimal HER activity among all samples, such as an ultralow overpotential of about 9.0 mV at the current density of 10.0 mA cm<sup>−2</sup>, which greatly surpasses HER activity of CoN<sub>2</sub>/Ru–NP (53.0 mV) or CoN<sub>4</sub>/Ru–NC (84.0 mV) and even is superior to that of Pt/C (ca. 24.0 mV). By comparison, we also test polarization curves of CoN<sub>2</sub> and CoN<sub>4</sub> (the characterizations of CoN<sub>4</sub> shown in Fig. S17), yielding the overpotentials of 224.0 mV for CoN<sub>2</sub> and 353.0 mV for CoN<sub>4</sub> at the same conditions (Fig. S18a). Here, to investigate the faradaic efficiencies of the as-synthesized samples, the producing H<sub>2</sub> from our working electrodes will be gathered using H<sub>2</sub>O draining technique to figure out the moles of experimentally detected H<sub>2</sub> [7]. On the other side, we utilize gas-chromatography (GC) method to analyze the purity of the produced gas. Accordingly, the faradaic efficiencies of CoN<sub>2</sub>/Ru–NC, CoN<sub>2</sub>/Ru–NP and CoN<sub>4</sub>/Ru–NC are 98.1 %, 96.5 % and 93.3 %, respectively (Fig. S19).

From this figure, CoN<sub>2</sub>/Ru–NC demonstrates the highest faradaic efficiency among all samples, being quite close to the theoretically available data. Besides, CoN<sub>2</sub>/Ru–NC exhibits the stable H<sub>2</sub> evolution rate, reaching up to 0.183 mmol h<sup>−1</sup>, which is higher than that of CoN<sub>2</sub>/Ru–NP (0.180 mmol h<sup>−1</sup>) or CoN<sub>4</sub>/Ru–NC (0.174 mmol h<sup>−1</sup>). In terms of Fig. S18b and Fig. 4b, Tafel plot of CoN<sub>2</sub>/Ru–NC, 45 mV dec<sup>−1</sup>, is much lower than Tafel plots of CoN<sub>2</sub>/Ru–NP (121 mV dec<sup>−1</sup>), CoN<sub>4</sub>/Ru–NC (141 mV dec<sup>−1</sup>) and Pt/C (55 mV dec<sup>−1</sup>), indicating faster electrode kinetics. Based on these results, the HER mechanism on CoN<sub>2</sub>/Ru–NC undertakes the Volmer–Heyrovsky mode while producing H<sub>2</sub> on CoN<sub>2</sub>/Ru–NP or CoN<sub>4</sub>/Ru–NC proceeds sluggish Volmer one. In consequence, the effect of the nitrogen–coordination number of Co–SAs and the existence form of Ru species on HER activity is in line with the DFT calculations (Fig. 1f). Subsequently, we investigate *R*<sub>CT</sub> of CoN<sub>2</sub>/Ru–NC, CoN<sub>2</sub>/Ru–NP, CoN<sub>4</sub>/Ru–NC, CoN<sub>2</sub> and CoN<sub>4</sub>. In our viewpoint, all samples possess low *R*<sub>CT</sub> (Fig. 4c). Since highly conducting carbon substrates are applied as “the expressway” to achieve efficient electron transfer for accelerating cathode kinetics [60,61]. On the other hand, the analysis of charge density difference is performed on CoN<sub>2</sub>/Ru–NC, CoN<sub>4</sub>/Ru–NC and CoN<sub>2</sub> (Fig. 4g–i). Interestingly, there is a significant electron accumulation at the interfaces between Co–SAs and Ru–NC for CoN<sub>2</sub>/Ru–NC or CoN<sub>4</sub>/Ru–NC from the side-view along the *b* axis (lower figure of Fig. 4g or h). Such electron accumulation facilitates charge transfer during HER [62]. In sharp contrast, no similar phenomenon is observed in CoN<sub>2</sub> from the side-view of Fig. 4i due to the absence of Ru species. Therefore, CoN<sub>2</sub>/Ru–NC, CoN<sub>4</sub>/Ru–NC and CoN<sub>2</sub>/Ru–NP demonstrate lower *R*<sub>CT</sub> than CoN<sub>2</sub> or CoN<sub>4</sub> (Fig. 4c). Undoubtedly, these results further imply that charge transfer is not the key factor to influence HER activities of CoN<sub>2</sub>/Ru–NC, CoN<sub>2</sub>/Ru–NP and CoN<sub>4</sub>/Ru–NC.

Boosting highly active sites is another critical factor to realize efficient HER. Following this opinion, the electrochemical active surface area is characterized by measuring *C*<sub>dl</sub> of the as-synthesized samples (Fig. 4d) originated from the CV curves (Fig. S20). From Fig. 4d, CoN<sub>2</sub>/Ru–NC exhibits higher *C*<sub>dl</sub> (107.3 mF cm<sup>−2</sup>) than CoN<sub>2</sub>/Ru–NP (40.1 mF cm<sup>−2</sup>) or CoN<sub>4</sub>/Ru–NC (33.6 mF cm<sup>−2</sup>), which indicates that there should be more active sites involved in electrocatalysis for CoN<sub>2</sub>/Ru–NC. Here, the specific HER activity (SHERA) is further assessed the intrinsic activity of each sample. The roughness factors (*R*<sub>f</sub>) is calculated by the following equation: *R*<sub>f</sub> = *C*<sub>dl</sub> *C*<sub>s</sub><sup>−1</sup>, where *C*<sub>s</sub> is regarded as the specific capacitance (40.0 μF cm<sup>−2</sup>). The related *R*<sub>f</sub> data are obtained, 2682 for CoN<sub>2</sub>/Ru–NC, 1002 for CoN<sub>2</sub>/Ru–NP and 840 for CoN<sub>4</sub>/Ru–NC (Fig. S21). Next, the intrinsic activity is figured out by the equation of SHERA = *j* *R*<sub>f</sub><sup>−1</sup>, where *j* is denoted as the current density [9,63]. Obviously, CoN<sub>2</sub>/Ru–NC demonstrates the highest SHERA among all samples from Fig. 4e. Therefore, it is concluded that CoN<sub>2</sub>/Ru–NC possesses not only richer active sites but also higher intrinsic activity than CoN<sub>2</sub>/Ru–NP or CoN<sub>4</sub>/Ru–NC.

To deeply elucidate the reason for excellent HER activity of CoN<sub>2</sub>/Ru–NC, we investigate their total, partial density of states (PDOS) and *ε*<sub>d</sub> (including Co and Ru), as shown in Fig. 4j–l. Considering that CoN<sub>2</sub>/Ru–NC and CoN<sub>4</sub>/Ru–NC possess the same Ru–NC but different Co–SAs, we rationally compare their Co *ε*<sub>d</sub>. From Fig. 4j, l, the Co *ε*<sub>d</sub> of CoN<sub>2</sub>/Ru–NC (−0.761 eV) is more negative than that of CoN<sub>4</sub>/Ru–NC (−0.745 eV), indicating the downshift in the Co *ε*<sub>d</sub> of CoN<sub>2</sub>/Ru–NC by decreasing the nitrogen–coordination number of Co–SAs in our strategy. According to the *d*-band theory, a high Co *ε*<sub>d</sub> for CoN<sub>4</sub>/Ru–NC indicates a strong binding interaction between the intermediates (H\*) and CoN<sub>4</sub> of CoN<sub>4</sub>/Ru–NC, leading to an unfavorable desorption of H\* [35]. Therefore, HER activity of CoN<sub>4</sub>/Ru–NC is inferior to that of CoN<sub>2</sub>/Ru–NC (Fig. 4a), conforming to theoretical prediction (Fig. 1f). Here, the analysis of charge density difference is conducted to uncover the effect of the nitrogen–coordination number on HER activity of CoN<sub>2</sub>/Ru–NC and CoN<sub>4</sub>/Ru–NC. For example, Co atom of CoN<sub>4</sub>/Ru–NC is yellow while the four N atoms connected to it are cyan from



the top-view along the *c* axis (upper figure of Fig. 4h). This indicates the electrons transfer from N atoms to Co atoms of CoN<sub>4</sub>/Ru-NC. However, such electron accumulation favors H<sup>+</sup> absorption rather than H<sup>+</sup> desorption from CoN<sub>4</sub>/Ru-NC. Instead, upper figure of Fig. 4g demonstrates electron transfer from CoN<sub>2</sub> to N atoms of CoN<sub>2</sub>/Ru-NC due to the electrons depletion on Co atom and the electron accumulation on two coordinated-N atoms. Therefore, the electron redistribution around Co-SAs is substantially induced by regulating the nitrogen-coordination number. Most important of all, such electron optimization weakens H<sup>+</sup> absorption, resulting in satisfactory  $\Delta G_H$  at Co sites of CoN<sub>2</sub>/Ru-NC for H<sup>+</sup> desorption.

One more thing, we further compare the Ru  $\epsilon_d$  of CoN<sub>2</sub>/Ru-NC with that of CoN<sub>2</sub>/Ru-NP. Of note is that anchoring Ru-NC on CoN<sub>2</sub>-containing substrates can robustly upshift the Ru  $\epsilon_d$ . For example, the Ru  $\epsilon_d$  of CoN<sub>2</sub>/Ru-NC reaches up to  $-2.822$  eV, being higher than that of CoN<sub>2</sub>/Ru-NP ( $-2.843$  eV) from Fig. 4j, k. This is because Ru metallic species with the small diameter will lead to low work function ( $\Phi$ ) value; low  $\Phi$  value is usually accompanied by a positive shift of the Ru  $\epsilon_d$  [64]. Therefore, as the size of nanoclusters decreases, the  $\epsilon_d$  of Ru gradually moves upwards. Together, a feasible strategy is for the first time developed to synergistically modulate  $\epsilon_d$  of bimetallic elements. In this strategy, the downshift in the Co  $\epsilon_d$  is realized by synthesizing CoN<sub>2</sub> at increasing *T* during the pyrolysis step while upshifting the Ru  $\epsilon_d$  is achieved via decreasing  $m_{Ru}$  to anchor Ru nanoclusters instead of nanoparticles on CoN<sub>2</sub>-containing carbon substrates toward the synthesis of CoN<sub>2</sub>/Ru-NC.

As we know, promoting the dissociation of H<sub>2</sub>O is also regarded as another important factor to realize efficient alkaline HER. This process includes the adsorption of H<sub>2</sub>O and Volmer step. Among them, the Volmer step consists of two stages: H<sub>2</sub>O dissociation into the adsorbed H atom (H<sup>\*</sup><sub>ad</sub>) and hydroxyl (OH<sup>\*</sup><sub>ad</sub>), as well as the transformation OH<sup>\*</sup><sub>ad</sub> into OH<sup>-</sup> and OH<sup>-</sup> desorbing off. Typically, the ruthenium-based

electrocatalysts promise the important application in alkaline HER owing to their strong capabilities for water dissociation [65,66]. To reveal the capabilities of water adsorption and dissociation of CoN<sub>2</sub>/Ru-NC, CoN<sub>2</sub>/Ru-NP and CoN<sub>4</sub>/Ru-NC, their contact angles (CAs), activation energies and Zeta potentials ( $\zeta$ ) are carefully explored in Fig. 5a–i. First, the as-synthesized samples almost show the same CAs which are less than 90° (Fig. 5a–c), indicating good hydrophilicity. All models about the adsorption of H<sub>2</sub>O, H<sub>2</sub>O dissociation into H<sup>\*</sup><sub>ad</sub> and OH<sup>\*</sup><sub>ad</sub> as well as the transition state (TS) are displayed in Fig. 5d–f, Fig. S22, 23. According to Fig. 5g, the values of energy change ( $\Delta E$ ) of the water adsorption on all models are negative, ranging from  $-0.39$  to  $-0.27$  eV (the detailed information in Table S5). These results directly imply that the water adsorption on each model is thermodynamically favorable. In addition, the energy of TS and energy barrier of the dissociation of H<sub>2</sub>O into H<sup>\*</sup><sub>ad</sub> and OH<sup>\*</sup><sub>ad</sub> for all models are also exhibited in Fig. 5h. From this figure and Table S6, CoN<sub>2</sub>/Ru-NC demonstrates not only the lowest energy TS (0.47 eV) but also the smallest energy barrier of the H<sub>2</sub>O dissociation (0.03 eV) among all models. This straightforwardly proves that the dissociation of H<sub>2</sub>O into H<sup>\*</sup><sub>ad</sub> and OH<sup>\*</sup><sub>ad</sub> on Ru-NC of CoN<sub>2</sub>/Ru-NC is more dynamically favorable than other samples. It can be rationally expounded as follows: the upshift in the Ru  $\epsilon_d$  (Fig. 4j, k) will upgrade its antibonding states, resulting in the enhanced affinity between Ru-NC and OH<sup>\*</sup><sub>ad</sub>. Therefore, such affinity lengthens the H-O bond of H<sub>2</sub>O to facilitate the dissociation of H<sub>2</sub>O into H<sup>\*</sup><sub>ad</sub> and OH<sup>\*</sup><sub>ad</sub>. Last but not least, OH<sup>-</sup> desorption is dependent on the  $\zeta$  of the electrocatalyst [67]. The low  $\zeta$  favors the transformation OH<sup>\*</sup><sub>ad</sub> into OH<sup>-</sup> as well as OH<sup>-</sup> desorbing off due to the strong repulsive force during alkaline HER [9,67]. As is shown in Fig. 5i, CoN<sub>2</sub>/Ru-NC also exhibits much lower  $\zeta$  ( $-20.0$  mV) than CoN<sub>2</sub>/Ru-NP ( $-14.4$  mV) and CoN<sub>4</sub>/Ru-NC ( $-17.7$  mV). It is not understood that OH<sup>-</sup> more easily desorbs off from CoN<sub>2</sub>/Ru-NC. Based on the above results, our strategy significantly accelerates the sluggish Volmer step of alkaline HER.

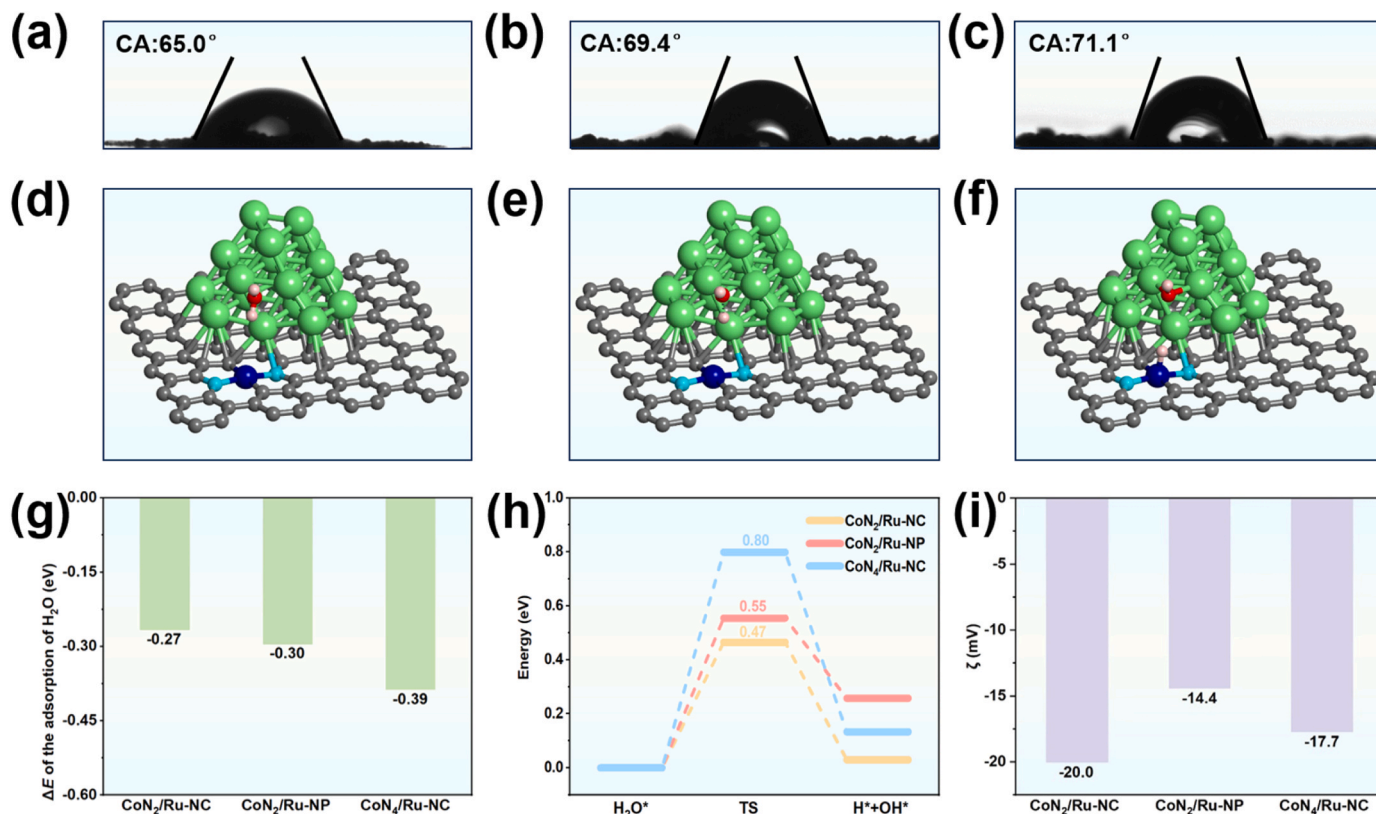


**Fig. 5.** CA measurements of (a) CoN<sub>2</sub>/Ru-NC (b) CoN<sub>2</sub>/Ru-NP and (c) CoN<sub>4</sub>/Ru-NC; Schematic illustration of models of (d) the adsorption of H<sub>2</sub>O, (e) TS and (f) the dissociation of H<sub>2</sub>O into H<sup>\*</sup><sub>ad</sub> and OH<sup>\*</sup><sub>ad</sub> on CoN<sub>2</sub>/Ru-NC for DFT calculations; (g)  $\Delta E$  of the adsorption of H<sub>2</sub>O, (h) energy barriers of the dissociation of H<sub>2</sub>O into H<sup>\*</sup><sub>ad</sub> and OH<sup>\*</sup><sub>ad</sub> on CoN<sub>2</sub>/Ru-NC, CoN<sub>2</sub>/Ru-NP and CoN<sub>4</sub>/Ru-NC; (i)  $\zeta$  of CoN<sub>2</sub>/Ru-NC, CoN<sub>2</sub>/Ru-NP and CoN<sub>4</sub>/Ru-NC. In (d-f), the red balls are O atoms.

Here, to further summarize the relationship between alkaline HER activity and such TMs  $\epsilon_d$  from the aspects of active sites and promoting  $\text{H}_2\text{O}$  dissociation, we construct plots of  $\Delta G_H$  at Co-SAs *versus* the Co  $\epsilon_d$  of  $\text{CoN}_2/\text{Ru-NC}$ ,  $\text{CoN}_2/\text{Ru-NP}$  and  $\text{CoN}_4/\text{Ru-NC}$  (Fig. 6a), as well as  $\Delta G_H$  at Ru atoms (site 2) and the dissociation energy barriers of the water on the surfaces of  $\text{CoN}_2/\text{Ru-NC}$  and  $\text{CoN}_2/\text{Ru-NP}$  *versus* the respective Ru  $\epsilon_d$  (Fig. 6b). As is shown in Fig. 6a, Co-SAs of  $\text{CoN}_4/\text{Ru-NC}$  demonstrate an unfavorable  $\Delta G_H$  (about  $-0.07$  eV) compared to those of  $\text{CoN}_2/\text{Ru-NC}$  ( $0.01$  eV). This is because the Co  $\epsilon_d$  of  $\text{CoN}_4/\text{Ru-NC}$  ( $-0.745$  eV) is closer to the Fermi level than that of  $\text{CoN}_2/\text{Ru-NC}$  ( $-0.761$  eV). Accordingly, such strong affinity between Co atoms of  $\text{CoN}_4/\text{Ru-NC}$  and  $\text{H}^*$  is responsible for having difficulty desorption of  $\text{H}_2$  (Fig. 6a). In terms of the *d*-band theory, down-regulation of the Co  $\epsilon_d$  is necessary, but not too low. For instance, the Co  $\epsilon_d$  of  $\text{CoN}_2/\text{Ru-NP}$  down-regulating to  $-0.765$  eV leads to a weak affinity between their Co atoms and  $\text{H}^*$ . Thus,  $\Delta G_H$  of  $\text{CoN}_2/\text{Ru-NP}$  is unsatisfactory either. At fine-tuning the Co  $\epsilon_d$  to  $-0.761$  eV,  $\text{CoN}_2/\text{Ru-NC}$  demonstrates the most satisfactory  $\Delta G_H$  among all samples (Fig. 6a). On the other hand, taking into account that  $\text{CoN}_2$ -containing substrates instead of  $\text{CoN}_4$ -containing ones are advantageous for providing catalytically newborn Co-SAs as active sites in this work, we synthesize  $\text{CoN}_2/\text{Ru-NC}$  and  $\text{CoN}_2/\text{Ru-NP}$  by anchoring Ru species on  $\text{CoN}_2$ -containing substrates to further investigate their Ru  $\epsilon_d$ . The related Ru  $\epsilon_d$  data are  $-2.843$  eV for  $\text{CoN}_2/\text{Ru-NP}$  and  $-2.822$  eV for  $\text{CoN}_2/\text{Ru-NC}$ . As is shown in Fig. 6b, up-regulating the Ru  $\epsilon_d$  is achieved via decreasing  $m_{\text{Ru}}$  to anchor Ru nanoclusters on  $\text{CoN}_2$ -containing

carbon substrates toward the synthesis of  $\text{CoN}_2/\text{Ru-NC}$ . Affirmatively,  $\Delta G_H$  at Ru atoms are far away from zero form Fig. 6b, which indicates these Ru atoms are not considered as active site for HER. More importantly, the effect of regulating the Ru  $\epsilon_d$  on the dissociation of  $\text{H}_2\text{O}$  is the major issue. Up-regulating the Ru  $\epsilon_d$  enhances the affinity between  $\text{OH}^*_{\text{ad}}$  and Ru atoms of  $\text{CoN}_2/\text{Ru-NC}$ , thus promoting the dissociation of  $\text{H}_2\text{O}$  into  $\text{H}^*_{\text{ad}}$  and  $\text{OH}^*_{\text{ad}}$  and quickening the sluggish Volmer step toward alkaline HER. According to these results and discussion, the effect of synergistic modulation of  $\epsilon_d$  of bimetallic elements on alkaline HER activity of the as-synthesized samples, or their possible electrocatalytic mechanism is demonstrated in Fig. 6c.

With these benefits,  $\text{CoN}_2/\text{Ru-NC}$  exhibits higher HER activity than most Ru-based electrocatalysts in the previously-reported literature (Fig. S24). Furthermore,  $\text{CoN}_2/\text{Ru-NC}$  demonstrates a reliable long-term durability (Fig. 4f). For example, there is a negligible degradation in polarization curves after 4000 cycles (Fig. 4f), and no obvious decrement after 24.0 h HER measurement at the current density of  $10 \text{ mA cm}^{-2}$  is observed in inset of Fig. 4f.

#### 4. Conclusion

In summary, a novel strategy has been proposed to design and synthesize Ru nanoclusters anchoring on carbon substrates which contains Co single atoms with low nitrogen-coordination number for activating Co atoms as catalytically newborn sites and promoting water dissociation toward synergistically accelerating alkaline HER. In our strategy,

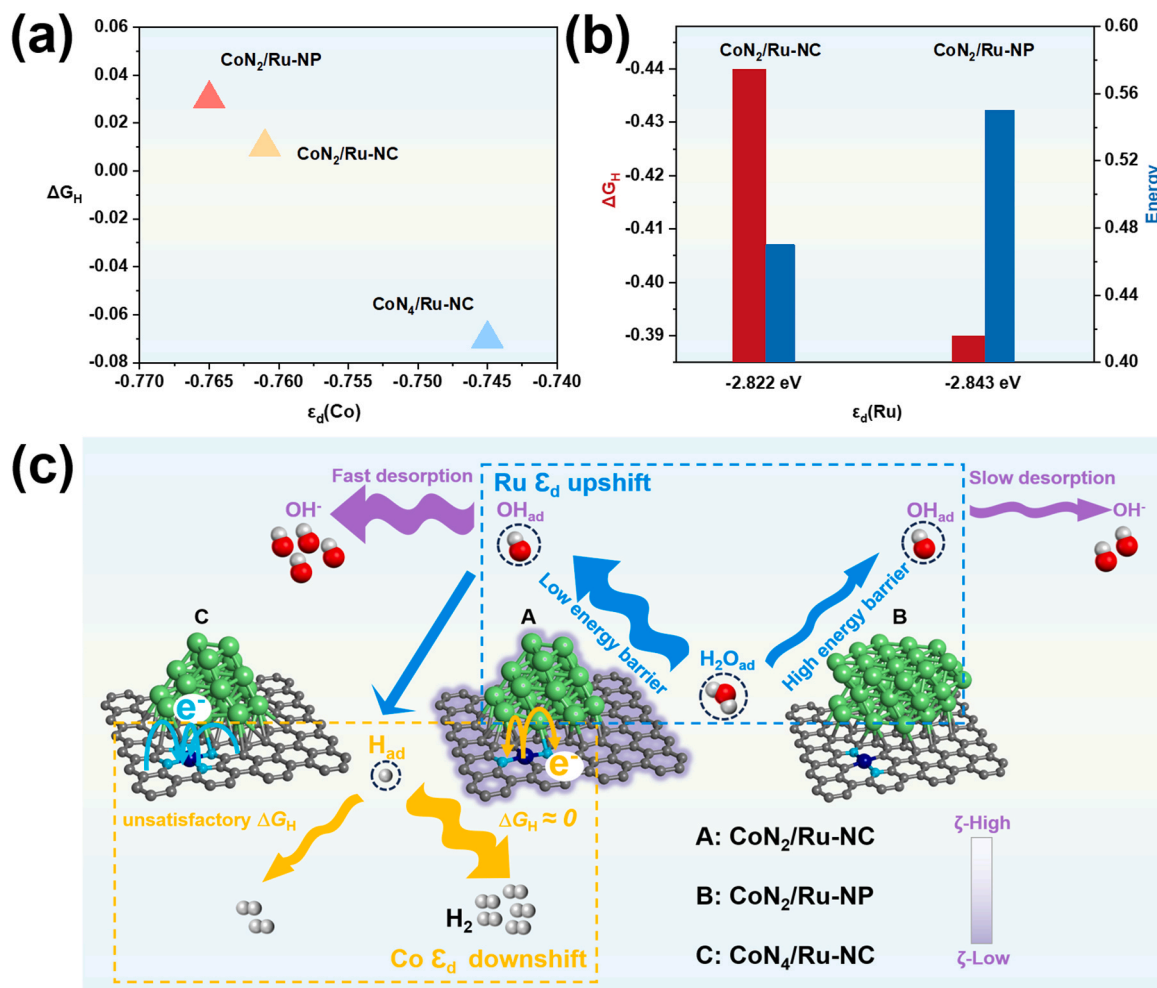


**Fig. 6.** (a) Relationship between  $\Delta G_H$  at Co-SAs and the Co  $\epsilon_d$  of  $\text{CoN}_2/\text{Ru-NC}$ ,  $\text{CoN}_2/\text{Ru-NP}$  and  $\text{CoN}_4/\text{Ru-NC}$ ; (b) Energy barriers of water dissociation and  $\Delta G_H$  at site 2 *versus* the Ru  $\epsilon_d$  of  $\text{CoN}_2/\text{Ru-NC}$  and  $\text{CoN}_2/\text{Ru-NP}$ ; (c) Possible electrocatalytic mechanism of  $\text{CoN}_2/\text{Ru-NC}$ ,  $\text{CoN}_2/\text{Ru-NP}$  and  $\text{CoN}_4/\text{Ru-NC}$ .

controlling the nitrogen-coordination number of Co–SAs and existence form Ru species can modulate Co and Ru  $\epsilon_d$  of the as-synthesized samples. The downshift in the Co  $\epsilon_d$  is realized by synthesizing Co single atoms with low nitrogen-coordination number at increasing  $T$  during the pyrolysis step while the upshift in the Ru  $\epsilon_d$  is carried out *via* decreasing the mass precursor to anchor Ru nanoclusters rather than nanoparticles on CoN<sub>2</sub>–containing carbon substrates. Interestingly, the downshift in Co  $\epsilon_d$  results in a satisfactory  $\Delta G_H$  at these Co–SAs to facilitate desorption of H<sub>2</sub>; in addition, the upshift in Ru  $\epsilon_d$  of CoN<sub>2</sub>/Ru–NC favors the adsorption of OH\* on Ru nanoclusters to promote water dissociation for highly efficient alkaline HER. With these benefits, CoN<sub>2</sub>/Ru–NC demonstrates an outstanding activity with an ultralow overpotential of  $\sim 9.0$  mV at  $10.0 \text{ mA cm}^{-2}$ , which suppresses activities of Pt/C ( $24.0$  mV) and most previously-reported Ru-based electrocatalysts. Our results provide a novel strategy for the design and synthesis of outstanding hybridized-electrocatalysts *via* synergistically modulating  $\epsilon_d$  of multiple TMs and present an insightful understanding of the possible mechanism on hydrogen spillover and accelerated water dissociation toward alkaline HER.

### CRediT authorship contribution statement

**Yu Li:** Investigation. **Jin-Ping Liu:** Investigation. **Cui-Fang Ye:** Investigation. **Yi-Long Wang:** Writing – review & editing, Writing – original draft, Supervision, Project administration, Conceptualization. **Shu-ming Li:** Writing – review & editing, Writing – original draft, Software, Methodology, Investigation, Data curation, Conceptualization. **Zhan Liu:** Writing – original draft, Software, Investigation, Data curation, Conceptualization. **Xiao-Yun Li:** Investigation. **Shen Yu:** Investigation. **Ming-Hui Sun:** Investigation. **Li-Hua Chen:** Writing – review & editing, Writing – original draft, Supervision, Project administration, Funding acquisition. **Bao-Lian Su:** Writing – review & editing, Writing – original draft, Supervision, Conceptualization.

### Declaration of Competing Interest

The authors declare that they have no known competing financial interests or personal relationships that could have appeared to influence the work reported in this paper.

### Data availability

Data will be made available on request.

### Acknowledgements

Li-hua Chen acknowledges the Hubei Provincial Department of Education for the “Chutian Scholar” program. This work was also financially supported by the National Natural Science Foundation of China (No. U20A20122). The authors deeply thank the 111 Projects (Grant No. B20002) and the International Science & Technology Cooperation Program of China (2021YFE0115800) for supporting this work.

### Appendix A. Supporting information

Supplementary data associated with this article can be found in the online version at [doi:10.1016/j.apcatb.2024.123972](https://doi.org/10.1016/j.apcatb.2024.123972).

### References

- [1] J.A. Turner, Sustainable hydrogen production, *Science* 305 (2004) 972–974, <https://doi.org/10.1126/science.1103197>.
- [2] T. Gao, X. Tang, X. Li, S. Wu, S. Yu, P. Li, D. Xiao, Z. Jin, Understanding the atomic and defective interface effect on ruthenium clusters for the hydrogen evolution reaction, *ACS Catal.* 13 (2023) 49–59, <https://doi.org/10.1021/acscatal.2c04586>.
- [3] D. Xue, J. Cheng, P. Yuan, B.-A. Lu, H. Xia, C.-C. Yang, C.-L. Dong, H. Zhang, F. Shi, S.-C. Mu, J.-S. Hu, S.-G. Sun, J.-N. Zhang, Boron-tethering and regulative electronic

- states around iridium species for hydrogen evolution, *Adv. Funct. Mater.* 32 (2022) 2113191, <https://doi.org/10.1002/adfm.202113191>.
- [4] Z. Wang, P. Guo, S. Cao, H. Chen, S. Zhou, H. Liu, H. Wang, J. Zhang, S. Liu, S. Wei, D. Sun, X. Lu, Contemporaneous inverse manipulation of the valence configuration to preferred Co<sup>2+</sup> and Ni<sup>3+</sup> for enhanced overall water electrocatalysis, *Appl. Catal. B- Environ.* 284 (2021) 119725, <https://doi.org/10.1016/j.apcatb.2020.119725>.
- [5] Y. Huang, X. Song, J. Deng, C. Zha, W. Huang, Y. Wu, Y. Li, Ultra-dispersed molybdenum phosphide and phosphosulfide nanoparticles on hierarchical carbonaceous scaffolds for hydrogen evolution electrocatalysis, *Appl. Catal. B- Environ.* 245 (2019) 656–661, <https://doi.org/10.1016/j.apcatb.2019.01.034>.
- [6] K. Song, H. Zhang, Z. Lin, Z. Wang, L. Zhang, X. Shi, S. Shen, S. Chen, W. Zhong, Interfacial engineering of cobalt thiophosphate with strain effect and modulated electron structure for boosting electrocatalytic hydrogen evolution reaction, *Adv. Funct. Mater.* (2023) 2312672, <https://doi.org/10.1002/adfm.202312672>.
- [7] Y. Liu, G. Yu, G.-D. Li, Y. Sun, T. Asefa, W. Chen, X. Zou, Coupling Mo<sub>2</sub>C with nitrogen-rich nanocarbon leads to efficient hydrogen-evolution electrocatalytic sites, *Angew. Chem. Int. Ed.* 54 (2015) 10752–10757, <https://doi.org/10.1002/anie.201504376>.
- [8] R. Paul, Q. Zhai, A.K. Roy, L. Dai, Charge transfer of carbon nanomaterials for efficient metal-free electrocatalysis, *Interdiscip. Mater.* 1 (2022) 28–50, <https://doi.org/10.1002/idm2.12010>.
- [9] Y. Meng, P. Zeng, X.-Y. Yang, Z. Liu, X.-Y. Li, C.-F. Ye, Y. Li, J.-P. Liu, B.-L. Su, L.-H. Chen, Y.-L. Wang, Simultaneously achieving enhanced water adsorption and rapid adsorbed hydroxyl transfer toward MXene-based materials for highly efficient alkaline electrocatalytic hydrogen evolution, *Chem. Eng. J.* 466 (2023) 143372, <https://doi.org/10.1016/j.cej.2023.143372>.
- [10] L. Zhang, J. Zhu, X. Li, S. Mu, F. Verpoort, J. Xue, Z. Kou, J. Wang, Nurturing the marriages of single atoms with atomic clusters and nanoparticles for better heterogeneous electrocatalysis, *Interdiscip. Mater.* 1 (2022) 51–87, <https://doi.org/10.1002/idm2.12011>.
- [11] P. Zeng, Y. Meng, Z. Liu, G.-Q. Sun, X.-Y. Li, X.-Y. Yang, C.-F. Ye, Y. Li, J.-P. Liu, L.-H. Chen, B.-L. Su, Y.-L. Wang, N-doping coupled with Co-vacancies activating sulfur atoms and narrowing bandgap for cos toward synergistically accelerating hydrogen evolution, *Small* 19 (2023) 2301279, <https://doi.org/10.1002/smll.202301279>.
- [12] W. Guo, Z. Wang, X. Wang, Y. Wu, General design concept for single-atom catalysts toward heterogeneous catalysis, *Adv. Mater.* 33 (2021) 2004287, <https://doi.org/10.1002/adma.202004287>.
- [13] L. An, J. Feng, Y. Zhang, R. Wang, H. Liu, G.-C. Wang, F. Cheng, P. Xi, Epitaxial heterogeneous interfaces on N-NiMoO<sub>4</sub>/NiS<sub>2</sub> nanowires/nanosheets to boost hydrogen and oxygen production for overall water splitting, *Adv. Funct. Mater.* 29 (2019) 1805298, <https://doi.org/10.1002/adfm.201805298>.
- [14] Y. Wang, M. Zhang, Z. Kang, L. Shi, Y. Shen, B. Tian, Y. Zou, H. Chen, X. Zou, Nano-metal diborides-supported anode catalyst with strongly coupled TaO<sub>x</sub>/IrO<sub>2</sub> catalytic layer for low-iridium-loading proton exchange membrane electrolyzer, *Nat. Commun.* 14 (2023) 5119, <https://doi.org/10.1038/s41467-023-40912-8>.
- [15] L. Yang, L. Shi, H. Chen, X. Liang, B. Tian, K. Zhang, Y. Zou, X. Zou, A highly active, long-lived oxygen evolution electrocatalyst derived from open-framework iridates, *Adv. Mater.* 35 (2023) 2208539, <https://doi.org/10.1002/adma.202208539>.
- [16] C. He, L. Yang, X. Peng, S. Liu, J. Wang, C. Dong, D. Du, L. Li, L. Bu, X. Huang, Alkylamine-confined thickness-tunable synthesis of Co(OH)<sub>2</sub>-CoO nanosheets toward oxygen evolution catalysis, *ACS Nano* 17 (2023) 5861–5870, <https://doi.org/10.1021/acsnano.2c12735>.
- [17] J. Li, C. Hou, C. Chen, W. Ma, Q. Li, L. Hu, X. Lv, J. Dang, Collaborative interface optimization strategy guided ultrafine RuCo and MXene heterostructure electrocatalysts for efficient overall water splitting, *ACS Nano* 17 (2023) 10947–10957, <https://doi.org/10.1021/acsnano.3c02956>.
- [18] E. Cao, Z. Chen, H. Wu, P. Yu, Y. Wang, F. Xiao, S. Chen, S. Du, Y. Xie, Y. Wu, Z. Ren, Boron-induced electronic-structure reformation of CoP nanoparticles drives enhanced pH-universal hydrogen evolution, *Angew. Chem. Int. Ed.* 59 (2020) 4154–4160, <https://doi.org/10.1002/anie.201915254>.
- [19] X. Luo, P. Ji, P. Wang, R. Cheng, D. Chen, C. Lin, J. Zhang, J. He, Z. Shi, N. Li, S. Xiao, S. Mu, Interface engineering of hierarchical branched Mo-doped Ni<sub>3</sub>S<sub>2</sub>/Ni<sub>x</sub>P<sub>y</sub> hollow heterostructure nanorods for efficient overall water splitting, *Adv. Energy Mater.* 10 (2020) 1903891, <https://doi.org/10.1002/aenm.201903891>.
- [20] M. Hu, H. Chen, B. Liu, X. Xu, B. Cao, P. Jing, J. Zhang, R. Gao, J. Zhang, Coupling ceria with dual-phased molybdenum carbides for efficient and stable hydrogen evolution electrocatalysis at large-current-density in freshwater and seawater, *Appl. Catal. B- Environ.* 317 (2022) 121774, <https://doi.org/10.1016/j.apcatb.2022.121774>.
- [21] D.R. Paudel, U.N. Pan, R.B. Ghising, M.R. Kandel, S. Prabhakaran, D.H. Kim, N. H. Kim, J.H. Lee, Multi-interfacial dendritic engineering facilitating congruous intrinsic activity of oxide-carbide/MOF nanostructured multimodal electrocatalyst for hydrogen and oxygen electrocatalysis, *Appl. Catal. B- Environ.* 331 (2023) 122711, <https://doi.org/10.1016/j.apcatb.2023.122711>.
- [22] Y. Zeng, Z. Cao, J. Liao, H. Liang, B. Wei, X. Xu, H. Xu, J. Zheng, W. Zhu, L. Cavallo, Z. Wang, Construction of hydroxide pn junction for water splitting electrocatalysis, *Appl. Catal. B- Environ.* 292 (2021) 120160, <https://doi.org/10.1016/j.apcatb.2021.120160>.
- [23] F. Guo, Y. Wu, H. Chen, Y. Liu, L. Yang, X. Ai, X. Zou, High-performance oxygen evolution electrocatalysis by boronized metal sheets with self-functionalized surfaces, *Energy Environ. Sci.* 12 (2019) 684–692, <https://doi.org/10.1039/C8EE03405B>.
- [24] X. Liang, L. Shi, Y. Liu, H. Chen, R. Si, W. Yan, Q. Zhang, G.-D. Li, L. Yang, X. Zou, Activating inert, nonprecious perovskites with iridium dopants for efficient oxygen



- evolution reaction under acidic conditions, *Angew. Chem. Int. Ed.* 58 (2019) 7631–7635, <https://doi.org/10.1002/anie.201900796>.
- [25] Z. Wu, B. Huang, X. Wang, C.-S. He, Y. Liu, Y. Du, W. Liu, Z. Xiong, B. Lai, Facilely tuning the first-shell coordination microenvironment in iron single-atom for Fenton-like chemistry toward highly efficient wastewater purification, *Environ. Sci. Technol.* 57 (2023) 14046–14057, <https://doi.org/10.1021/acs.est.3c04343>.
- [26] X. Zhao, G. Wu, X. Zheng, P. Jiang, J.-D. Yi, H. Zhou, X. Gao, Z.-Q. Yu, Y. Wu, A double atomic-tuned RuBi SAA/Bi@OG nanostructure with optimum charge redistribution for efficient hydrogen evolution, *Angew. Chem. Int. Ed.* 62 (2023) e202300879, <https://doi.org/10.1002/anie.202300879>.
- [27] X. Lin, Z. Zhou, Q.-Y. Li, D. Xu, S.-Y. Xia, B.-L. Leng, G.-Y. Zhai, S.-N. Zhang, L.-H. Sun, G. Zhao, J.-S. Chen, X.-H. Li, Direct oxygen transfer from H<sub>2</sub>O to cyclooctene over electron-rich RuO<sub>2</sub> nanocrystals for epoxidation and hydrogen evolution, *Angew. Chem. Int. Ed.* 61 (2022) e202207108, <https://doi.org/10.1002/anie.202207108>.
- [28] Y. Lu, C. Yue, Y. Li, W. Bao, X. Guo, W. Yang, Z. Liu, P. Jiang, W. Yan, S. Liu, Y. Pan, Y. Liu, Atomically dispersed ni on Mo<sub>2</sub>C embedded in N, P co-doped carbon derived from polyoxometalate supramolecule for high-efficiency hydrogen evolution electrocatalysis, *Appl. Catal. B- Environ.* 296 (2021) 120336, <https://doi.org/10.1016/j.apcatb.2021.120336>.
- [29] Q. Liu, K. Vandewal, Understanding and suppressing non-radiative recombination losses in non-fullerene organic solar cells, *Adv. Mater.* 35 (2023) 2302452, <https://doi.org/10.1002/adma.202302452>.
- [30] T. Wu, Z. Xu, X. Wang, M. Luo, Y. Xia, X. Zhang, J. Li, J. Liu, J. Wang, H.-L. Wang, F. Huang, Surface-confined self-reconstruction to sulfate-terminated ultrathin layers on NiMo<sub>3</sub>S<sub>4</sub> toward biomass molecule electro-oxidation, *Appl. Catal. B- Environ.* 323 (2023) 122126, <https://doi.org/10.1016/j.apcatb.2022.122126>.
- [31] Y. Hu, Z. Li, Z. Wang, X. Wang, W. Chen, J. Wang, W. Zhong, R. Ma, Suppressing local dendrite hotspots via current density redistribution using a superlithiophilic membrane for stable lithium metal anode, *Adv. Sci.* 10 (2023) 2206995, <https://doi.org/10.1002/advs.202206995>.
- [32] B. Hammer, J.K. Norskov, Why gold is the noblest of all the metals, *Nature* 376 (1995) 238–240, <https://doi.org/10.1038/376238a0>.
- [33] S. Sun, X. Zhou, B. Cong, W. Hong, G. Chen, Tailoring the d-band centers endows (Ni<sub>4</sub>Fe<sub>1-x</sub>)<sub>2</sub>P nanosheets with efficient oxygen evolution catalysis, *ACS Catal.* 10 (2020) 9086–9097, <https://doi.org/10.1021/acscatal.0c01273>.
- [34] Y. Liu, Z. Zhang, L. Zhang, Y. Xia, H. Wang, H. Liu, S. Ge, J. Yu, Manipulating the d-band centers of transition metal phosphides through dual metal doping towards robust overall water splitting, *J. Mater. Chem. A* 10 (2022) 22125–22134, <https://doi.org/10.1039/D2TA04951A>.
- [35] J.-T. Ren, Y.-S. Wang, Y.-J. Song, L. Chen, Z.-Y. Yuan, Interface engineering of in-situ formed nickel hydr(oxy)oxides on nickel nitrides to boost alkaline hydrogen electrocatalysis, *Appl. Catal. B- Environ.* 309 (2022) 121279, <https://doi.org/10.1016/j.apcatb.2022.121279>.
- [36] B.-A. Lu, L.-F. Shen, J. Liu, Q. Zhang, L.-Y. Wan, D.J. Morris, R.-X. Wang, Z.-Y. Zhou, G. Li, T. Sheng, L. Gu, P. Zhang, N. Tian, S.-G. Sun, Structurally disordered phosphorus-doped Pt as a highly active electrocatalyst for an oxygen reduction reaction, *ACS Catal.* 11 (2021) 355–363, <https://doi.org/10.1021/acscatal.0c03137>.
- [37] Y. Wu, J. Cai, Y. Xie, S. Niu, Y. Zang, S. Wu, Y. Liu, Z. Lu, Y. Fang, Y. Guan, X. Zheng, J. Zhu, X. Liu, G. Wang, Y. Qian, Regulating the interfacial electronic coupling of Fe<sub>2</sub>N via orbital steering for hydrogen evolution catalysis, *Adv. Mater.* 32 (2020) 1904346, <https://doi.org/10.1002/adma.201904346>.
- [38] F. Podjaski, D. Weber, S. Zhang, L. Diehl, R. Eger, V. Duppel, E. Alarcón-Lladó, G. Richter, F. Haase, A. Fontcuberta i Morral, C. Scheu, B.V. Lotsch, Rational strain engineering in delafossite oxides for highly efficient hydrogen evolution catalysis in acidic media, *Nat. Catal.* 3 (2020) 55–63, <https://doi.org/10.1038/s41929-019-0400-x>.
- [39] W. Xu, G. Fan, J. Chen, J. Li, L. Zhang, S. Zhu, X. Su, F. Cheng, J. Chen, Nanoporous palladium hydride for electrocatalytic N<sub>2</sub> reduction under ambient conditions, *Angew. Chem. Int. Ed.* 59 (2020) 3511–3516, <https://doi.org/10.1002/anie.201914335>.
- [40] Y.-X. Guo, M. Yang, Z. Liu, X.-Y. Yang, Y. Xiao, X.-Y. Li, C.-F. Ye, Y. Li, J.-P. Liu, B.-L. Su, L.-H. Chen, Y.-L. Wang, Boosting highly active defect Mo<sup>v</sup> sites for amorphous molybdenum sulfide from catalyst-substrate effect toward efficient hydrogen evolution, *Electrochim. Acta* 449 (2023) 142191, <https://doi.org/10.1016/j.electacta.2023.142191>.
- [41] X. Zhu, X. Tan, K.-H. Wu, S.-C. Haw, C.-W. Pao, B.-J. Su, J. Jiang, S.C. Smith, J.-M. Chen, R. Amal, X. Lu, Intrinsic ORR activity enhancement of Pt atomic sites by engineering the d-band center via local coordination tuning, *Angew. Chem.* 133 (2021) 22082–22088, <https://doi.org/10.1002/ange.202107790>.
- [42] S. Peng, F. Gong, L. Li, D. Yu, D. Ji, T. Zhang, Z. Hu, Z. Zhang, S. Chou, Y. Du, S. Ramakrishna, Necklace-like multishelled hollow spinel oxides with oxygen vacancies for efficient water electrolysis, *J. Am. Chem. Soc.* 140 (2018) 13644–13653, <https://doi.org/10.1021/jacs.8b05134>.
- [43] J. Jin, J. Yin, H. Liu, B. Huang, Y. Hu, H. Zhang, M. Sun, Y. Peng, P. Xi, C.-H. Yan, Atomic sulfur filling oxygen vacancies optimizes H absorption and boosts the hydrogen evolution reaction in alkaline media, *Angew. Chem. Int. Ed.* 60 (2021) 14117–14123, <https://doi.org/10.1002/anie.202104055>.
- [44] C.-T. Dinh, A. Jain, F.P.G. de Arquer, P. De Luna, J. Li, N. Wang, X. Zheng, J. Cai, B. Z. Gregory, O. Voznyy, B. Zhang, M. Liu, D. Sinton, E.J. Crumlin, E.H. Sargent, Multi-site electrocatalysts for hydrogen evolution in neutral media by destabilization of water molecules, *Nat. Energy* 4 (2019) 107–114, <https://doi.org/10.1038/s41560-018-0296-8>.
- [45] W. Zhu, W. Chen, H. Yu, Y. Zeng, F. Ming, H. Liang, Z. Wang, NiCo/NiCo–OH and NiFe/NiFe–OH core shell nanostructures for water splitting electrocatalysis at large currents, *Appl. Catal. B- Environ.* 278 (2020) 119326, <https://doi.org/10.1016/j.apcatb.2020.119326>.
- [46] J.-T. Ren, X.-M. Wu, T. Liu, L. Chen, R. Hao, Y.-J. Song, Y.-P. Liu, Z.-Y. Yuan, Interfacial nickel with molybdenum oxides as monolithic catalyst to accelerate alkaline hydrogen electrocatalysis with robust stability, *Appl. Catal. B- Environ.* 317 (2022) 121786, <https://doi.org/10.1016/j.apcatb.2022.121786>.
- [47] Y. Zhao, P.V. Kumar, X. Tan, X. Lu, X. Zhu, J. Jiang, J. Pan, S. Xi, H.Y. Yang, Z. Ma, T. Wan, D. Chu, W. Jiang, S.C. Smith, R. Amal, Z. Han, X. Lu, Modulating Pt–O–Pt atomic clusters with isolated cobalt atoms for enhanced hydrogen evolution catalysis, *Nat. Commun.* 13 (2022) 2430, <https://doi.org/10.1038/s41467-022-30155-4>.
- [48] X. Wang, Z. Chen, X. Zhao, T. Yao, W. Chen, R. You, C. Zhao, G. Wu, J. Wang, W. Huang, J. Yang, X. Hong, S. Wei, Y. Wu, Y. Li, Regulation of coordination number over single Co sites: triggering the efficient electroreduction of CO<sub>2</sub>, *Angew. Chem. Int. Ed.* 57 (2018) 1944–1948, <https://doi.org/10.1002/anie.201712451>.
- [49] P. Yin, T. Yao, Y. Wu, L. Zheng, Y. Lin, W. Liu, H. Ju, J. Zhu, X. Hong, Z. Deng, G. Zhou, S. Wei, Y. Li, Single cobalt atoms with precise N-coordination as superior oxygen reduction reaction catalysts, *Angew. Chem. Int. Ed.* 55 (2016) 10800–10805, <https://doi.org/10.1002/anie.201604802>.
- [50] X. Liang, W. Yan, Y. Yu, K. Zhang, W. An, H. Chen, Y. Zou, X. Zhao, X. Zou, Electrocatalytic water oxidation activity-stability maps for perovskite oxides containing 3d, 4d and 5d transition metals, *Angew. Chem. Int. Ed.* 62 (2023) e202311606, <https://doi.org/10.1002/anie.202311606>.
- [51] Y. Cao, H. Lu, B. Xu, W. Yang, Q. Hong, Nitrogen/sulfur dual-doped porous carbon nanofibers with Co<sub>9</sub>S<sub>8</sub> nanoparticles encapsulated by graphitic shells: a highly active stable free-standing air electrode for rechargeable non-aqueous Li–O<sub>2</sub> batteries and primary alkaline Al–air batteries, *Chem. Eng. J.* 378 (2019) 122247, <https://doi.org/10.1016/j.cej.2019.122247>.
- [52] Y. Chen, R. Gao, S. Ji, H. Li, K. Tang, P. Jiang, H. Hu, Z. Zhang, H. Hao, Q. Qu, X. Liang, W. Chen, J. Dong, D. Wang, Y. Li, Atomic-level modulation of electronic density at cobalt single-atom sites derived from metal–organic frameworks: enhanced oxygen reduction performance, *Angew. Chem. Int. Ed.* 60 (2021) 3212–3221, <https://doi.org/10.1002/anie.202012798>.
- [53] B. Song, H. Zhao, G. Zhao, H. Li, C. Ge, G. Yan, J. Fang, Bifunctional carbon nanofibrous interlayer embedded with cobalt single atoms for polysulfides trapping and catalysis in lithium-sulfur batteries, *Chem. Eng. J.* 460 (2023) 141907, <https://doi.org/10.1016/j.cej.2023.141907>.
- [54] Y. Pan, R. Lin, Y. Chen, S. Liu, W. Zhu, X. Cao, W. Chen, K. Wu, W.-C. Cheong, Y. Wang, L. Zheng, J. Luo, Y. Lin, Y. Liu, C. Liu, J. Li, Q. Lu, X. Chen, D. Wang, Q. Peng, C. Chen, Y. Li, Design of single-atom Co–N<sub>5</sub> catalytic site: a robust electrocatalyst for CO<sub>2</sub> reduction with nearly 100% CO selectivity and remarkable stability, *J. Am. Chem. Soc.* 140 (2018) 4218–4221, <https://doi.org/10.1021/jacs.8b00814>.
- [55] W. Wang, Y. Wu, T. Liu, Y. Zhao, Y. Qu, R. Yang, Z. Xue, Z. Wang, F. Zhou, J. Long, Z. Yang, X. Han, Y. Lin, M. Chen, L. Zheng, H. Zhou, X. Lin, F. Wu, H. Wang, Y. Yang, Y. Li, Y. Dai, Y. Wu, Single Co sites in ordered SiO<sub>2</sub> channels for boosting nonoxidative propane dehydrogenation, *ACS Catal.* 12 (2022) 2632–2638, <https://doi.org/10.1021/acscatal.1c05921>.
- [56] P. Su, W. Pei, X. Wang, Y. Ma, Q. Jiang, J. Liang, S. Zhou, J. Zhao, J. Liu, G.Q. Lu, Exceptional electrochemical HER performance with enhanced electron transfer between Ru nanoparticles and single atoms dispersed on a carbon substrate, *Angew. Chem. Int. Ed.* 60 (2021) 16044–16050, <https://doi.org/10.1002/anie.202103557>.
- [57] Y. Liu, X. Li, Q. Zhang, W. Li, Y. Xie, H. Liu, L. Shang, Z. Liu, Z. Chen, L. Gu, Z. Tang, T. Zhang, S. Lu, A general route to prepare low-ruthenium-content bimetallic electrocatalysts for pH-universal hydrogen evolution reaction by using carbon quantum dots, *Angew. Chem. Int. Ed.* 59 (2020) 1718–1726, <https://doi.org/10.1002/anie.201913910>.
- [58] S. Yuan, Z. Pu, H. Zhou, J. Yu, I.S. Amini, J. Zhu, Q. Liang, J. Yang, D. He, Z. Hu, G. Van Tendeloo, S. Mu, A universal synthesis strategy for single atom dispersed cobalt/metal clusters heterostructure boosting hydrogen evolution catalysis at all pH values, *Nano Energy* 59 (2019) 472–480, <https://doi.org/10.1016/j.nanoen.2019.02.062>.
- [59] C. Hu, E. Song, M. Wang, W. Chen, F. Huang, Z. Feng, J. Liu, J. Wang, Partial-single-atom, partial-nanoparticle composites enhance water dissociation for hydrogen evolution, *Adv. Sci.* 8 (2021) 2001881, <https://doi.org/10.1002/advs.202001881>.
- [60] T. Lian, X. Li, Y. Wang, S. Zhu, X. Yang, Z. Liu, C. Ye, J. Liu, Y. Li, B. Su, L. Chen, Boosting highly active exposed Mo atoms by fine-tuning S-vacancies of MoS<sub>2</sub>-based materials for efficient hydrogen evolution, *ACS Appl. Mater. Interfaces* 14 (2022) 30746–30759, <https://doi.org/10.1021/acsaami.2c05444>.
- [61] Y.-I. Wang, Q. Huang, G.-q. Sun, X.-y. Li, L.-h. Chen, B.-l. Su, J.-p. Liu, Synergistic zinc doping and defect engineering toward MoS<sub>2</sub> nanosheet arrays for highly efficient electrocatalytic hydrogen evolution, *Dalton Trans.* 50 (2021) 5770–5775, <https://doi.org/10.1039/D0DT04207B>.
- [62] X. Hao, X. Zhang, Y. Xu, Y. Zhou, T. Wei, Z. Hu, L. Wu, X. Feng, J. Zhang, Y. Liu, D. Yin, S. Ma, B. Xu, Atomic-scale insights into the interfacial charge transfer in a NiO/CeO<sub>2</sub> heterostructure for electrocatalytic hydrogen evolution, *J. Colloid Interface Sci.* 643 (2023) 282–291, <https://doi.org/10.1016/j.jcis.2023.04.023>.
- [63] X.-Y. Li, S.-J. Zhu, Y.-L. Wang, T. Lian, X.-Y. Yang, C.-F. Ye, Y. Li, B.-L. Su, L.-H. Chen, Synergistic regulation of S-vacancy of MoS<sub>2</sub>-based materials for highly efficient electrocatalytic hydrogen evolution, *Front. Chem.* 10 (2022), <https://doi.org/10.3389/fchem.2022.915468>.
- [64] Q. Hu, K. Gao, X. Wang, H. Zheng, J. Cao, L. Mi, Q. Huo, H. Yang, J. Liu, C. He, Subnanometric Ru clusters with upshifted d band center improve performance for

- alkaline hydrogen evolution reaction, *Nat. Commun.* 13 (2022) 3958, <https://doi.org/10.1038/s41467-022-31660-2>.
- [65] C. Zhao, J. Wang, Y. Gao, J. Zhang, C. Huang, Q. Shi, S. Mu, Q. Xiao, S. Huo, Z. Xia, J. Zhang, X. Lu, Y. Zhao, D-orbital manipulated ru nanoclusters for high-efficiency overall water splitting at industrial-level current densities, *Adv. Funct. Mater.* 34 (2024) 2307917, <https://doi.org/10.1002/adfm.202307917>.
- [66] F. Zhu, J. Xue, L. Zeng, J. Shang, S. Lu, X. Cao, B.F. Abrahams, H. Gu, J. Lang, One-pot pyrolysis synthesis of highly active Ru/RuO<sub>x</sub> nanoclusters for water splitting, *Nano Res* 15 (2022) 1020–1026, <https://doi.org/10.1007/s12274-021-3590-x>.
- [67] B. Mao, P. Sun, Y. Jiang, T. Meng, D. Guo, J. Qin, M. Cao, Identifying the transfer kinetics of adsorbed hydroxyl as a descriptor of alkaline hydrogen evolution reaction, *Angew. Chem. Int. Ed.* 59 (2020) 15232–15237, <https://doi.org/10.1002/anie.202006722>.